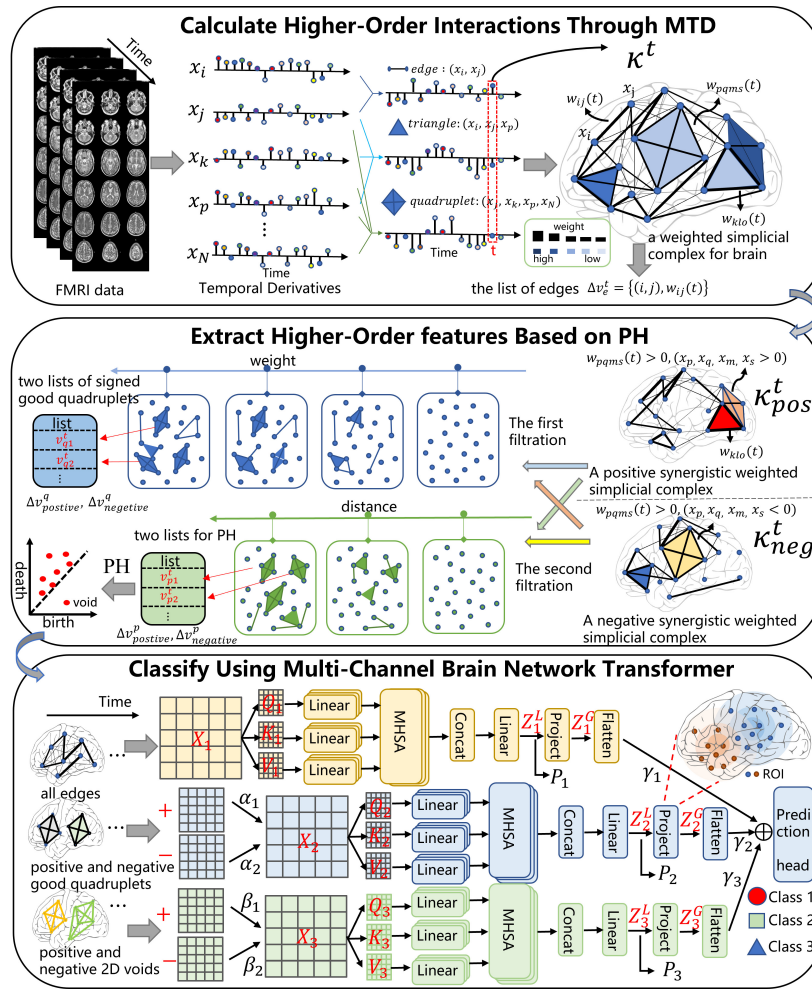


# Graphical Abstract

## Signed Higher-Order Interactions for Brain Disorder Diagnosis via Multi-Channel Transformers

Dengyi Zhao, Zhiheng Zhou, Guiying Yan, Dongxiao Yu, Xingqi Qi



## Highlights

### **Signed Higher-Order Interactions for Brain Disorder Diagnosis via Multi-Channel Transformers**

Dengyi Zhao, Zhiheng Zhou, Guiying Yan, Dongxiao Yu, Xingqi Qi

- A novel metric - Multiplication of Temporal Derivatives (MTD) - for quantifying dynamic functional co-fluctuations of group ROIs is proposed.
- The first utilization of quadruplet-level interaction signatures and two-dimensional void descriptors extracted by Persistent Homology in the brain enhances diagnostic efficacy.
- To the best of our knowledge, this is the first attempt to distinguish between positively and negatively synergistic higher-order interactions.
- A novel multi-channel brain network Transformer is proposed to synergistically integrate lower-order edge features with the higher-order topological invariants.

# Signed Higher-Order Interactions for Brain Disorder Diagnosis via Multi-Channel Transformers

Dengyi Zhao<sup>a</sup>, Zhiheng Zhou<sup>b</sup>, Guiying Yan<sup>b</sup>, Dongxiao Yu<sup>c</sup>, Xingqi Qi<sup>a,\*</sup>

<sup>a</sup>*School of Mathematics and Statistics, Shandong  
University, Weihai, 264209, Shandong, China*

<sup>b</sup>*Academy of Mathematics and Systems Science, Chinese Academy of  
Sciences, Beijing, 100190, Beijing, China*

<sup>c</sup>*School of Computer Science and Technology, Shandong  
University, Qingdao, 266000, Shandong, China*

---

## Abstract

Accurately characterizing the higher-order interactions of brain regions and effectively extracting the interpretable higher-order organizational patterns in Functional Magnetic Resonance Imaging (fMRI) data are crucial for the diagnosis of brain diseases. However, current graph models based on deep learning mainly focus on pairwise patterns, as well as triadic patterns within brain while overlooking more higher-order patterns with signs, limiting an integrated understanding of brain-wide communication. To address these challenges, we propose HOI-Brain (Higher-Order Interaction in Brain Network), a novel computational framework that enables the utilization of signed higher-order interactions and signed organizational patterns in fMRI data for the diagnosis of brain diseases. Specifically, we present a new calculation of co-fluctuations based on Multiplication of Temporal Derivatives to detect higher-order interactions with adequate temporal resolution. Next, we further distinguish positively and negatively synergistic higher-order interactions and encode them in signed weighted simplicial complexes, which can offer detailed insights into the communication within the brain. Moreover, founded upon Persistent Homology theory, two distinct filtration processes are employed in weighted simplicial complexes of the brain to extract signed

---

\*Corresponding author.

*Email addresses:* zhaodengyi@mail.sdu.edu.cn (Dengyi Zhao),  
zhouzhiheng@amss.ac.cn (Zhiheng Zhou), yangy@amt.ac.cn (Guiying Yan),  
dxyu@sdu.edu.cn (Dongxiao Yu), qixingqin@sdu.edu.cn (Xingqi Qi)

higher-dimensional neural organisations from a spatiotemporal perspective. Finally, a multi-channel brain Transformer architecture is proposed to holistically integrate information from heterogeneous topological features. Comprehensive experiments across Alzheimer’s disease, Parkinson’s syndrome, and autism spectrum disorder datasets demonstrate the superiority, effectiveness, and interpretability of our framework. The extracted key brain regions and higher-order organizational patterns have been demonstrated to align reliably with domain knowledge from the neuroscience scientific literature, thereby providing direct and meaningful insights. Our code is available.

*Keywords:* Brain network, higher-order interaction, Transformer, fMRI biomarker, persistent homology theory

---

## 1. Introduction

Functional Magnetic Resonance Imaging (fMRI) is one of the key tools in neuroscience to discover potential neuroimaging biomarkers for the automated diagnosis of brain disorders, including Alzheimer’s disease (AD), autism spectrum disorder (ASD), and Parkinson’s disease (PD) (Lindquist, 2008; Fornito et al., 2016). Specifically, resting state fMRI measures functional connectivity between brain regions via blood-oxygen-level-dependent (BOLD) signals. This process naturally models the brain as a network, defining regions of interest (ROIs) as nodes and functional connections between ROIs as edges (Sporns, 2010; Bullmore and Sporns, 2009). Abnormalities in this network at the whole brain level are expected to yield disease-related biomarker signatures (Wang et al., 2021).

A significant number of graph data mining methodologies are then applied to such brain networks for brain disorder diagnosis, with the goal of understanding and analysing the elements and interactions of neurological systems from a network perspective. Examples include graph neural network (GNN)-based models (Xia et al., 2025), brain Transformer-based models (Kan et al., 2022b), hypergraph neural network (HGNN)-based models (Wang et al., 2024a), and persistent homology (PH)-based models (Bian et al., 2023). Although these studies have demonstrated the considerable potential of network based approaches in elucidating the complexities of the brain and diagnosing brain disorders, graph analysis of brain networks remains an emerging field in its infancy (Fotiadis et al., 2024).

Recently, graph neural network (GNN) techniques have been employed to

analyse brain networks characterised by pairwise interactions. These methods facilitate the extraction of potential topological features that are instrumental in diagnosing brain disorders (Luo et al., 2024). Several GNN-based models specifically designed for brain networks—including GroupINN (Yan et al., 2019), BrainGNN (Li et al., 2021), FBNetGen (Kan et al., 2022a), BPI-GNN (Zheng et al., 2024), and ASD-HNet (Luo et al., 2025)—have been proposed and have achieved promising diagnostic performance. It is generally accepted that GNN-based models use a message passing mechanism in which the embedding of a brain ROI is updated by aggregating information from its neighbouring ROIs, thereby learning a discriminative graph-level representation of the brain connectivity network. However, these methods are limited by the underlying assumption that interactions between nodes are strictly pairwise. Growing evidence indicates that the complexity of brain-region interactions extends far beyond pairwise connections, with widespread co-fluctuations occurring in groups of nodes that evolve over time (Battiston et al., 2020; Chelaru et al., 2021). Consequently, the limited expressiveness of traditional GNNs prevents them from capturing higher-order interactions in brain networks, and the topological features they extract are typically regarded as lower-order.

Transformer-based brain network models have achieved tremendous success in diagnosing brain disorders, thanks to their ability to capture global patterns. Representative examples include Graph Transformer (Ying et al., 2021), Brain Network Transformer (Kan et al., 2022b), TSEN (Hu et al., 2023), and Long-range Brain Transformer (Yu et al., 2024). These models naturally construct fully connected graphs and, through a powerful global attention mechanism, adaptively learn pairwise interaction relationships for brain disorder diagnosis. However, they typically use either the raw time series features of brain regions or the functional connectivity matrix as node-level input, thereby overlooking significant higher-order topological information among ROIs.

Several studies have focused on representing higher-order interactions (HOIs) in brain networks with more sophisticated models—primarily hypergraphs, thereby improving diagnostic performance for brain diseases (Jie et al., 2016; Xiao et al., 2019; Wang et al., 2022; Hao et al., 2023; Wang et al., 2024a). Although HGNN-based models have shown promising results by characterising HOIs via hyperedges generated through  $k$ -nearest-neighbour or  $k$ -hop neighbourhoods, this node-centric construction scheme conflicts with the notion of group dependence, as it fails to capture gen-

uine simultaneous interactions among groups of ROIs. Moreover, it has been demonstrated that higher-order features extracted by HGNN-based models can obscure their relationship to specific topological or neurobiological phenomena (Kim et al., 2024; Su et al., 2024).

To extract more interpretable higher-order topological features for brain-disorder diagnosis, recent studies have adopted persistent homology (PH), a topological approach capable of reconstructing HOI structures and delivering state-of-the-art performance in characterising brain topological profiles (Hyekyoung et al., 2011; Sizemore et al., 2018). However, most investigations of higher-order structures in brain networks have focused on 0-dimensional (connected components) and 1-dimensional (cycles) topological profiles formed by nodes and edges; these dimensions do not link HOIs in the brain to higher-order organisations that would provide a truly higher-dimensional perspective (Talesh Jafadideh and Mohammadzadeh Asl, 2022; Bian et al., 2024; Bhattacharya et al., 2025). To address this limitation, researchers have recently leveraged synchronisation phenomena to construct more accurate simplicial complexes for modelling HOIs and have used PH to capture 1-dimensional cycles that reflect triplet interactions (Santoro et al., 2024). Comprehensive analyses demonstrate that methods incorporating inferred higher-order interactions among three ROIs outperform traditional pairwise approaches, thereby offering new insights into the higher-order organisation of fMRI time-series data. Nevertheless, evidence shows that triplet interactions can be decomposed into linear combinations of pairwise interactions if they are linearly decomposable, implying that some triplets may not represent genuine higher-order phenomena (Delabays et al., 2025; Neuhäuser et al., 2020). Consequently, considering even higher-order interactions and organisational structures could yield deeper understanding of brain function. Moreover, existing measures of instantaneous co-fluctuation rely on extended Pearson correlation, which lacks the temporal resolution required to detect spatiotemporal interactions among groups of regions (Shine et al., 2015). Finally, the role of signed HOIs—potentially informative for neurological conditions—has been largely overlooked in these studies.

To address these methodological challenges, we propose an innovative computational framework, HOI-Brain (Higher-Order Interactions in Brain), that enables a comprehensive analysis of HOIs in fMRI data (Fig. 1). First, we introduce a novel metric—Multiplication of Temporal Derivatives (MTD)—to quantify dynamic functional co-fluctuations among groups of ROIs. MTD computes element-wise products of the temporal derivatives

of blood-oxygen-level-dependent (BOLD) signals, yielding instantaneous co-fluctuation magnitudes for  $k$ -node interactions. This approach more reliably identifies genuine higher-order neural interactions than Pearson’s correlation. Second, adopting a spatiotemporal analytic perspective, we model brain networks as weighted simplicial complexes that link instantaneous co-fluctuation of  $k$  node interactions in the brain to the weight of  $k$ -simplex, which can accommodate more information about interactions among multi-ROIs compared to pairwise networks. We further extract positively and negatively synergistic interactions from the weighted simplicial complexes to construct two signed weighted simplicial complexes, respectively. Positively synergistic interactions reflect multiple brain regions that exhibit simultaneous activation at a given moment relative to the preceding one, while negatively synergistic interactions indicate that these regions collectively exhibit inhibition at the current moment compared to the prior moment, which can offer detailed information about complex coordination and communication within the brain, thus improving the effectiveness of brain disease diagnosis. We further explore the influence of signed higher-order interactions (HOIs) using the self-attention mechanism. Through two distinct filtration processes based on Persistent Homology theory, we systematically extract four types of higher-order topological features: (1) positive and negative quadruplet-level interaction signatures that capture irreducible higher-order neural coordination patterns and (2) positive and negative two-dimensional void descriptors that characterize the intrinsic geometric organization of neural activity from a higher-dimensional manifold perspective. Third, given the significance of both lower-order interactions and higher-order interactions in brain network analysis tasks, we develop a multi-channel brain network Transformer to synergistically integrate lower-order edge features with the above four types of higher-order topological invariants. Specifically, we inject higher-order information into a multi-channel Transformer and use an orthonormal clustering readout operation based on self-supervised soft clustering and orthonormal projection to learn distinguishable cluster-aware lower- and higher-order node embeddings. Then we use an attention mechanism to adaptively fuse the features encoded by different channels. Finally, we utilize MLP as prediction head to classify the different levels of topological features extracted from the multi-channel brain network Transformer.

Experiments on Alzheimer’s disease, autism spectrum disorder, and Parkinson’s disease datasets have demonstrated its superiority over 20 state-of-the-art baselines. The present study employs an ablation approach to demon-

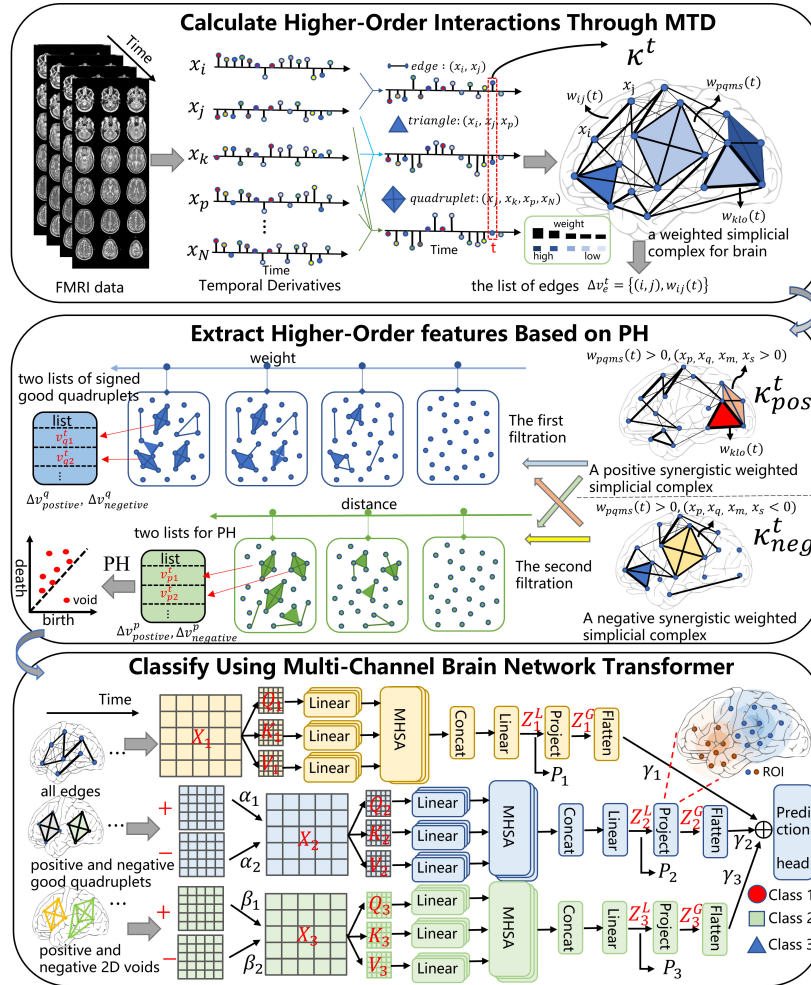


Figure 1: Overall framework of HOI-Brain. Individual fMRI data are transformed into  $N$  original fMRI signals through a preprocessing pipeline. A novel metric - Multiplication of Temporal Derivatives (MTD) - is quantified dynamic functional co-fluctuations of group ROIs. Then, at each timepoint  $t$ , some instantaneous  $k$ -order co-fluctuation time series are encoded into two signed weighted simplicial complexes respectively. Persistent Homology are applied to analyze the two signed weighted simplicial complexes at each  $t$ . Five feature matrices are generated by extracting all edges, signed good quadruplets, and signed 2D voids. These matrices are temporally averaged across all timepoints to stabilize feature feature representations. By incorporating the lower-order and higher-order feature, a multi-channel brain network transformer is using to produce the final classification.

strate the significance of higher-order topological features, the efficacy of distinct components of the proposed model, and the superiority of quadruplet interactions over triplet interactions in enhancing the diagnostic efficacy of brain diseases. Next, by visualizing the attention scores in the self-attention mechanism, the importance of signed information and channel information was identified. This finding indicates that the integration of positive and negative information, in conjunction with higher-order and low-order interactions within brain networks, can remarkably enhance diagnostic performance in a range of brain disease diagnostic tasks. Furthermore, by visualising the self-attention maps in the multi-channel brain network Transformer, interaction patterns among disease-related key brain regions and key interactions between ROIs were identified from a more comprehensive brain network perspective. In addition, we uncover some higher-order organizational patterns associated with specific stages of disease progression based on our methods.

In general, this study makes four contributions.

1. A novel metric - Multiplication of Temporal Derivatives (MTD) - for quantifying dynamic functional co-fluctuations of group ROIs is proposed. This approach employs element-wise products of temporal derivatives of blood oxygen level-dependent (BOLD) signals to represent instantaneous co-fluctuation magnitudes of  $k$  node interactions, which can achieve reliable identification of genuine higher-order neural interactions compared to pearson correlation.
2. The first utilization of quadruplet-level interaction signatures and two-dimensional void descriptors in the brain enhances diagnostic efficacy, providing a higher-dimensional perspective for studying higher-order brain structures compared to one-dimensional cycles.
3. To the best of our knowledge, this is the first attempt to distinguish between positively and negatively synergistic higher-order interactions, which may offer valuable insights into the complex coordination and communication within the brain, thereby improving the effectiveness of brain disease diagnosis.
4. A novel multi-channel brain network Transformer is proposed to synergistically integrate lower-order edge features with the higher-order topological invariants.

The contributions made in this work illustrate the potential of quadruplet or greater-order region interactions in improving the diagnostic efficacy

of brain diseases and advancing the understanding of brain networks and neurodegenerative diseases.

## 2. Related work

### 2.1. Graph models based on deep learning

A significant number of graph models are then applied to brain networks for the purpose of brain disorder diagnosis, with the objective being to understand and analyse the elements and interactions of neurological systems from a network perspective. Graph neural networks (GNNs) have been demonstrated to be particularly effective in modelling brain connectomes, due to their ability to effectively capture subtle, latent representations and nonlinear relationships in graph-structured data. Several GNN-based models, specifically designed for brain networks, have been proposed and have achieved promising diagnostic performance. For instance, GroupINN (Yan et al., 2019) incorporates the concept of node grouping into the neural network and designs a random-walk-based variant of graph convolutional layer. BrainGNN (Li et al., 2021) designs novel ROI-aware graph convolutional (Ra-GConv) layers that leverage the topological and functional information of fMRI. FB-NETGEN (Kan et al., 2022a) utilizes a task-aware GNN-based framework for fMRI analysis via functional brain network generation, which generates the brain connectivity matrices and predicts clinical outcomes simultaneously from fMRI BOLD signal series. BPI-GNN (Zheng et al., 2024) analyzes functional magnetic resonance images (fMRI) by leveraging the well-known prototype learning method. ASD-HNNet (Luo et al., 2025) designs a hybrid neural network model for ASD identification, which hierarchically extracts features from functional brain networks at threescales: local ROI scale, community scale, and global representation scale. However, these methods are essentially based on a two-way network to model pairwise interactions and mine low-order topological features for the diagnosis of brain disorders, overlooking the influence of HOIs in the brain.

Additionally, with advancements in large language models, transformer-based methods are increasingly being integrated into brain graph structures. Graph transformer (Ying et al., 2021) can be applied to brain networks to learn pairwise connection strengths among ROIs across individuals. Then, Brain Network Transformer (Kan et al., 2022b) leverages the unique properties of brain network data to fully unleash the power of Transformer-based models for brain network analysis, which avoids the costly computations of

eigenvalues or eigenvectors. TSEN (Hu et al., 2023) introduced snowball graph convolution as position embedding in Transformer structure, which was a simple yet effective method for capturing local patterns of brain naturally. Long-range Brain Transformer (Yu et al., 2024) injects the long-range embeddings into a transformer framework and integrate both short-range and long-range dependencies between ROIs using the self-attention mechanism. These works ignore significant high-order topological information among ROIs.

Some studies have been made in constructing HOIs in the brain to improve the performance of brain disorder diagnosis based on hypergraphs. For example, a novel framework (Jie et al., 2016) is proposed to estimate the hyperconnectivity network of brain functions for the diagnosis of brain disease. MHL-Hypergraph (Xiao et al., 2019) proposes a multi-hypergraph learning based method to compute a unified hypergraph similarity matrix from multi-paradigm fMRI data to represent an FCN for each subject. An evolving hypergraph convolutional network (Wang et al., 2022) for the dynamic hyperbrain network is proposed, which adds the attention mechanism to further enhance the ability of representation learning. To consider the temporal characteristics of longitudinal data, a weighted hypergraph convolution network (WHGCN) (Hao et al., 2023) is designed to use the internal correlations among different time points and leverage high-order relationships between subjects for AD detection. CcSi-MHAHGEL (Wang et al., 2024a) introduced a new hypergraph convolution network framework to extract multiatlas-based FCN embeddings with application to multisite ASD identification, where hyperedge-aware HGCN was developed to capture complex high order information in brain network. These studies primarily use  $k$ -nearest neighbour or  $k$ -hop neighbour constructions to generate hypergraphs, which are inconsistent with the definition of group dependence in brain regions. Furthermore, higher-order features extracted using hypergraph neural networks (HGNNs) are frequently regarded as being less interpretable.

## 2.2. Persistent Homology on brain connectome

Persistent homology (PH) is a widely used effective algebraic topological tool for the analysis of the brain connectome, enabling the capture of more interpretable high-order topological features. Rather than attempting to determine a single optimal threshold, researchers (Hyekyoung et al., 2011) suggest examining the topological changes in the brain network as

the threshold is increased continuously based on persistent homology. Researchers (Sizemore et al., 2018) also highlight the importance of cliques and cavities in the human connectome and locate topological cavities of different dimensions, around which information may flow in either diverging or converging patterns. To address the difficult issue of functional connectivity network (FCN) comparison across different spatiotemporal resolutions, researchers (Cassidy et al., 2018) develop a novel network comparison framework based on persistent homology to observe the change of 0-dimensional homology group. Besides, researchers (Bian et al., 2024) propose an adversarially trained persistent homology-based graph convolutional network (ATPGCN) to capture disease-specific brain connectome patterns for brain disorder diagnosis. Researchers (Bhattacharya et al., 2025) use the persistent topological features of connected components (H0) and loops (H1), which are quantified by two methods: Vietoris-Rips filtration and graph filtration, for diagnosing brain disorders. However, these studies ignore the importance of 2-dimensional topological profiles (i.e., voids), and do not links HOIs in the brain to these higher-order organisations. Recently, researchers (Santoro et al., 2024) have adopted certain methodologies grounded in the synchronisation phenomenon to construct more accurate simplicial complexes for modeling HOIs and use PH to capture 1-dimensional cycles related to triplet interactions. However, this can easily generate a large number of false positive high-order interactions and overlook higher-order quadruplet interactions with adequate temporal resolution. Besides, the influence of signed HOIs was overlooked in these studies, which could offer a broader diagnostic view of neurological conditions.

### 3. Method

The task of diagnosing brain disorders primarily involves inferring specific properties (represented as class labels) from functional magnetic resonance imaging (fMRI) data in the form of graphs. Given a labeled dataset  $\mathcal{D} = \{(\mathcal{G}, \mathcal{Y})\} = \{(G_i, y_i)\}_{i=1}^N$ , where each graph  $G_i \in \mathcal{G}$  corresponds to a label  $y_i \in \mathcal{Y}$ , the goal is to extract features to train a mapping function  $f_\theta : \mathcal{G} \rightarrow \mathcal{Y}$  that generalizes to unobserved graphs. For example, in studies of Alzheimer’s disease using brain networks, the label space comprises three diagnostic categories: NC (Normal Control), MCI (Mild Cognitive Impairment) and AD (Alzheimer’s Disease). The objective is to extract both lower-order and higher-order topological features from annotated brain net-

work data in order to learn a robust classifier  $f_\theta$ , ensuring its effectiveness on novel, unseen brain connectomes.

### 3.1. Signed Higher-Order Interaction Representation Strategy

Most traditional network neuroscience approaches construct functional connectivity through pairwise Pearson correlations of fMRI time series (Fornito et al., 2016; Lindquist, 2008). Recent edge-centric frameworks account for interactions of edges by computing instantaneous co-fluctuations through element-wise products of  $z$ -scored signals  $\mathbf{x}_i \odot \mathbf{x}_j$  (Faskowitz et al., 2020). Reference (Santoro et al., 2023, 2024) extended this approach to characterize  $k$ -order interactions when  $k + 1$  nodes simultaneously deviate from their temporal mean activation at time  $t$ . Although these techniques based on Pearson correlations have provided insights into the brain’s dynamic higher-order interactions, the methods have generally been limited by the lack of adequate temporal resolution (Shine et al., 2015). Now we give a new way to calculate co-fluctuations between several ROIs.

#### 3.1.1. Calculate Co-fluctuation Through Multiplication of Temporal Derivatives

Considering the above observation, we propose a novel method for estimating instantaneous co-fluctuation magnitudes by incorporating the Multiplication of Temporal Derivatives (Shine et al., 2015). Let us consider an  $N$ -dimensional real-valued time series  $\{x_i(t)\}_{i=1}^N$  with  $T$  time points, where  $\mathbf{x}_i = [x_i(1), x_i(2), \dots, x_i(T)]$  represents the generic time series recorded from brain region  $i$ . We first calculate the temporal derivative  $\dot{x}_i$  of each time series  $\mathbf{x}_i$  by performing a first-order differencing:

$$\dot{x}_i(t - 1) = x_i(t) - x_i(t - 1) \quad (1)$$

for  $t = 2, 3, \dots, T$ . We normalize each data point by dividing the temporal derivative  $\dot{x}_i(t)$  by its standard deviation  $\sigma$ , computed over the entire time course. This normalization yields the new time series  $q_i(t)$ , expressed as:

$$q_i(t) = \frac{\dot{x}_i(t)}{\sigma_{\dot{x}_i}} \quad (2)$$

where  $\sigma_{\dot{x}_i}$  denotes the standard deviation of  $\dot{x}_i(t)$ . Subsequently, the generic element at time  $t$  of the  $z$ -scored  $k$ -order co-fluctuation among  $k + 1$  new

time series is calculated as:

$$\xi_{0\dots k}(t) = \frac{\prod_{m=0}^k q_m(t) - \mu \left[ \prod_{m=0}^k q_m \right]}{\sigma \left[ \prod_{m=0}^k q_m \right]}, \quad (3)$$

where  $\mu[\cdot]$  and  $\sigma[\cdot]$  represent the time-averaged mean and standard deviation functions, respectively. To differentiate concordant group interactions from discordant ones in a  $k$ -order product, concordant signs are always positively mapped, while discordant signs are negatively mapped. Formally,

$$\text{sign} [\xi_{0\dots k}(t)] = \begin{cases} +1 & \text{if } q_0(t), \dots, q_k(t) \text{ are all non-negative or non-positive,} \\ -1 & \text{otherwise.} \end{cases} \quad (4)$$

In other words, the weight  $w_{0\dots k}(t)$  at time  $t$  of the  $k$ -order co-fluctuations is defined as

$$w_{0\dots k}(t) = \text{sign} [\xi_{0\dots k}(t)] |\xi_{0\dots k}(t)|. \quad (5)$$

If we compute all possible products up to order  $k$ , this will result in  $\binom{N}{k+1}$  different co-fluctuation time series for each order  $k$ . In this paper, we focus on co-fluctuations up to dimension  $k = 3$  to capture quadruplet interactions. In this way, the Multiplication of Temporal Derivatives allows us to clarify the precise dynamic relationships among ROIs with better temporal precision than Pearson correlation coefficients.

### 3.1.2. Construct weighted simplicial complexes

For each temporal instance  $t$ , we also integrate multi-order co-fluctuations into a weighted simplicial complex  $\mathcal{K}^t$ . Formally, a  $(d - 1)$ -dimensional simplex  $\sigma$  is defined as a collection of  $d$  vertices, expressed as  $\sigma = \{p_0, p_1, \dots, p_{d-1}\}$ . A simplicial complex  $\mathcal{K}$  satisfies the closure condition: every face of a simplex in  $\mathcal{K}$  must also belong to  $\mathcal{K}$ . This structure is enhanced through weight assignments, where numerical values quantify interaction intensities across different simplex dimensions. The resulting framework provides temporal resolution to the evolving patterns of coordinated (and uncoordinated) group-level neural dynamics observed in fMRI signals.

### 3.1.3. Construct two signed weighted simplicial complexes

We must note that in a weighted simplicial complex  $\mathcal{K}^t$ , there are two kinds of signs of a simplex, the concordant signs of positive and the discordant

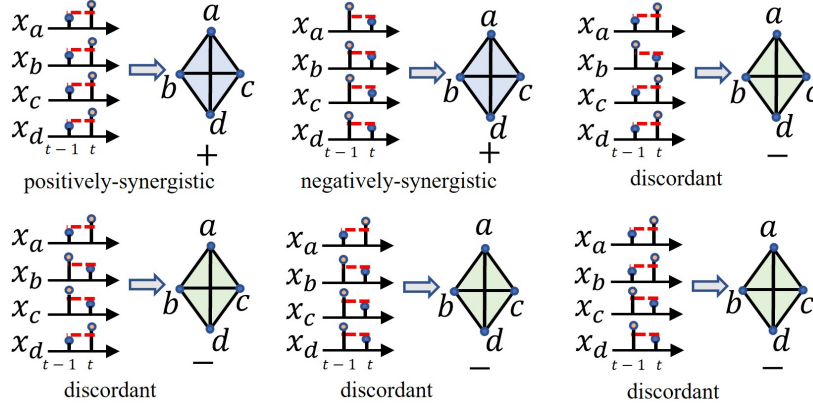


Figure 2: The illustration of six different signed quadruplet higher-order interactions.

signs of negative. We focus only on the concordant signs of positive but not on the discordant signs of negative because they may represent a confusing redundancy of information across multiple brain regions (Santoro et al., 2023). We further categorized the concordant interactions into positively-synergistic interactions and negatively-synergistic interactions. Positively synergistic interactions reflect multiple brain regions that exhibit simultaneous activation at a given moment relative to the preceding one, while negatively synergistic interactions indicate that these regions collectively exhibit inhibition at the current moment compared to the prior moment, which can offer valuable information about complex coordination and communication within the brain, thus improving the effectiveness of brain disease diagnosis. As shown in Fig. 2, it displays six different signed quadruplet higher-order interactions. For each temporal instance  $t$ , we further extract positively- and negatively-synergistic interactions from the weighted simplicial complexes to construct two signed weighted simplicial complexes  $\mathcal{K}_{positive}^t$  and  $\mathcal{K}_{negative}^t$ , respectively.

### 3.2. Topological Higher-order and Lower-order organization of FMRI signals

Many studies have explored higher-order structures in brain networks by focusing on loops (1D cycles) formed by nodes and edges (Bian et al., 2024; Bhattacharya et al., 2025). Besides, the influence of signed HOIs was overlooked in these studies, which could offer a broader diagnostic view of neurological conditions. Our proposed strategy for representing signed HOIs allows researchers to explore more complex signed higher-order structures,

such as quadriplet structures and voids (2D holes) formed by triangular faces. This advance is significant because it further refines the HOIs by defining sign and links HOIs in the brain to higher-order organisations, and provides a higher-dimensional perspective for studying higher-order structures in the brain, potentially providing new insights into brain organisation and function.

### 3.2.1. Filtrate the Weighted Simplicial Complexes

To mine the topological higher-order and lower-order organization of fMRI signals, we employ Persistent Homology (Talesh Jafadideh and Mohammadzadeh Asl, 2022), a computational topology technique adept at analyzing high-dimensional datasets. The core concept involves constructing a filtration—a sequence of simplicial complexes that progressively approximate the original weighted simplicial complex with increasing precision:

$$\emptyset = \mathcal{S}^0 \subset \mathcal{S}^1 \subset \dots \subset \mathcal{S}^l \subset \dots \subset \mathcal{S}^n. \quad (6)$$

In our study, we construct two distinct filtrations for the signed weighted simplicial complexes  $\mathcal{K}_{positive}^t$  and  $\mathcal{K}_{negative}^t$ . One filtration aims to extract all signed higher-order "good" quadruplets structures from the signed weighted simplicial complex. These structures represent co-fluctuations that are not observable through lower-order interactions alone. The other filtration is designed to identify signed 2-dimensional holes, which reflect the intrinsic shape of the data from a higher-dimensional perspective. Additionally, we also extract all lower-order edge structures from the weighted simplicial complex  $\mathcal{K}^t$ .

**The first filtration.** Sort the weights of edges, triangles, and quadruplets in ascending order for the signed weighted simplicial complexes. The parameter  $\epsilon_l \in \mathbb{R}$  scans this sequence, effectively tracking the current weight as we progress through the sorted list. At each step  $l$ , we identify all quadruplets that satisfy the simplicial downward closure condition, i.e., for each quadruplet  $(i, j, k, p)$ , the following conditions hold:

$$\forall (i, j, k, p) \in \Delta v^q, \quad w_{ijkp} > w_{ijk}, \quad w_{ijk} > w_{ij}, \quad (7)$$

where  $w_{ijkp}$ ,  $w_{ijk}$ , and  $w_{ij}$  denote the weights of the quadruplet, triangle, and edge, respectively. These quadruplets, along with their corresponding weights, are added to the signed list of "good" quadruplets  $\Delta v_{positive}^q =$

$\{(i, j, k, p), w_{ijkp}\}$  and  $\Delta v_{negative}^q = \{(i, j, k, p), w_{ijkp}\}$ . Additionally, all edges are added to the list of edges  $\Delta v_e = \{(i, j), w_{ij}\}$ .

**The second filtration.** Sort the weights of edges, triangles, and quadruplets in descending order for the signed weighted simplicial complexes. At each step  $l$ , we include all triangles and quadruplets that satisfy the simplicial upward closure condition. These triangles and quadruplets and all edges, along with their corresponding weights, are added to the signed list of persistent homology  $\Delta v_{positive}^p = \{(i, j, k, p), (1 - w_{ijkp})\}$  and  $\Delta v_{negative}^p = \{(i, j, k, p), (1 - w_{ijkp})\}$ .

Persistent homology examines how higher-order topological features evolve through the filtration  $\{\mathcal{S}^l\}$ , offering a measure of their robustness across scales. By focusing on 2D voids within the homology group  $H_2$ , we track these higher-order organization. Specifically, we apply Persistent Homology to the signed list of persistent homology  $\Delta v_{positive}^p$  and  $\Delta v_{negative}^p$  to generate two two-dimensional persistence diagrams. In each diagram, each point  $(b_g, d_g)$  signifies a void  $g$  that emerges during the filtration process. The persistence  $\pi_g = d_g - b_g$  quantifies the void's lifespan, indicating its importance.

To better quantify the higher-order topological features captured by persistence homology, we employ a homological scaffold (Petri et al., 2014), a weighted network representing the topological features in the persistence diagram. This scaffold comprises all voids corresponding to generators  $g_i$ , weighted by their persistence  $\pi_{g_i}$ . Specifically, if an edge  $e$  belongs to multiple two-dimensional voids  $g_0, g_1, \dots, g_s$ , its weight  $\bar{w}_e^\pi$  is defined as the sum of the persistences of these generators:

$$\bar{w}_e^\pi = \sum_{g_i | e \in g_i} \pi_{g_i}. \quad (8)$$

The homological scaffold reveals the roles of different links in shaping the system's homological properties. A larger total persistence  $\bar{w}_e^\pi$  for a link  $e$  indicates its function as a locally strong bridge within the space of coherent and decoherent co-fluctuations. To analyze the information from the signed list of "good" quadruplets  $\Delta v_{positive}^q$  and  $\Delta v_{negative}^q$  at the edge levels, we use edge projections (Barrat et al., 2004). For each edge  $(i, j)$ , we assign a weight  $w_{ij}$  equal to the average sum of the weights of the quadruplets defined by that edge. The feature matrices of 2D voids using homological scaffold and the feature matrices of quadruplet signatures using edge projections are illustrated in Fig. 3.

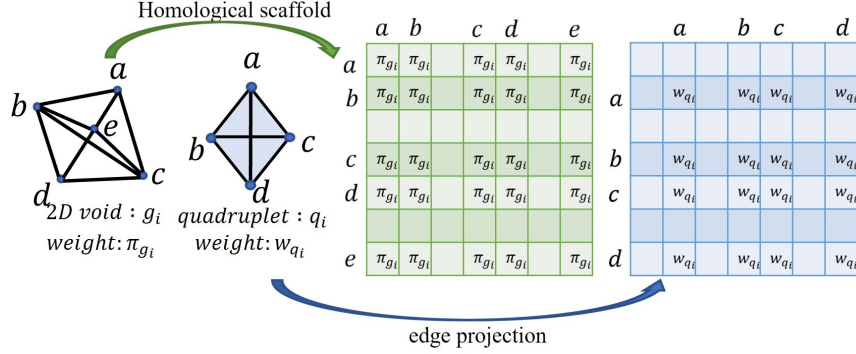


Figure 3: The illustration of the feature matrixes of 2D voids using homological scaffold and the feature matrixes of quadruplet signatures using edge projections.

At each time point  $t$ , five distinct weighted networks are constructed: one derived from edge structures representing lower-order interactions, two from signed good tetrahedral structures signifying higher-order interactions, and another two from signed 2D holes illustrating the data’s intrinsic geometric shape from a higher-dimensional perspective. By averaging across the entire time period, the resulting networks exhibit enhanced stability and mitigate the impact of fMRI noise.

### 3.2.2. Homological scaffold and edge projections

### 3.3. Multi-Channel Brain Network Transformer

To holistically integrate complementary information from heterogeneous topological features while preserving channel-specific properties, we propose a multi-channel brain network Transformer architecture with four coherently designed components.

#### 3.3.1. Signed High-order Features Decoupling Mechanism

High-order features that are positive are related to patterns of simultaneous activation in multiple brain regions at a given moment, while high-order features that are negative are related to patterns of collective inhibition in these regions at the current moment. These features can offer valuable information about complex coordination and communication within the brain. We further explore the influence of signed higher-order features using high-order features decoupling mechanism. Specifically, for each type of high-order feature’s two signed weighted adjacency matrix  $A_i^q, A_i^p \in \mathbb{R}^{N \times N}$  ( $i = 1, 2$ ), we

extract its upper triangular part and flatten it to construct a feature vector  $h_i^q, h_i^p \in \mathbb{R}^{N(N-1)/2}$ . We generate two new high-order topological features by adaptively learning weights to aggregate positive and negative information:

$$\alpha_1, \alpha_2 = \text{Softmax}(f^q(h_1^q, h_2^q)) \quad (9)$$

$$\tilde{A}^q = \alpha_1 \odot A_1^q + \alpha_2 \odot A_2^q \quad (10)$$

$$\beta_1, \beta_2 = \text{Softmax}(f^p(h_1^p, h_2^p)) \quad (11)$$

$$\tilde{A}^p = \beta_1 \odot A_1^p + \beta_2 \odot A_2^p \quad (12)$$

where  $f^q, f^p$  denotes a two-layer multi-layer perceptron (MLP), respectively, and  $\tilde{A}^q, \tilde{A}^p$  denotes features of quadruplet structures and that aggregate positive and negative information, respectively. The attention score  $\alpha_i, \beta_i$  emphasizes discriminative signed features while suppressing redundant signed information.

### 3.3.2. Multi-Head Self-Attention Module of Multiple Channels

The feature matrixes extracted above actually represents the low-order and high-order topological information associated with each brain region. Simply concatenating the low-order and high-order information of each brain region as the input to the model would overlook the heterogeneity of the related information. Therefore, inspired by Brain network Transformer (Kan et al., 2022b), we leverage a  $L$ -layer non-linear mapping module, namely Multi-Head Self-Attention (MHSA), to generate more expressive node features using the low-order and high-order topological features of multiple channels  $Z_i^l = \text{MHSA}(A_i) \in \mathbb{R}^{N \times N}$ , ( $i = 1, 2, 3$ ). For each layer  $l$ , the output of each channel  $Z_i^l$  is obtained by

$$Z_i^l = \left\| \prod_{m=1}^M h_i^{l,m} \right\| W_{O,i}^l \quad (13)$$

$$h_i^{l,m} = \text{Softmax} \left( \frac{\left( W_{Q,i}^{l,m} Z_i^{l-1} \right) \left( W_{K,i}^{l,m} Z_i^{l-1} \right)^\top}{\sqrt{d_{K,i}^{l,m}}} \right) W_{V,i}^{l,m} Z_i^{l-1} \quad (14)$$

where  $Z_i^0 = A_i$ ,  $\|\cdot\|$  is the concatenation operator,  $M$  is the number of heads,  $l$  is the layer index,  $W_O^l, W_{Q,i}^{l,m}, W_{K,i}^{l,m}, W_{V,i}^{l,m}$  are learnable model parameters of each channel, and  $d_{K,i}^{l,m}$  is the first dimension of  $\mathbf{W}_{K,i}^{l,m}$ .

### 3.3.3. Orthonormal Clustering Readout of Multiple Channels

Research has shown that low-level and high-level feature patterns in the brain often exhibit distinct functional modular structures, thereby supporting the richest functional interactions (Wang et al., 2019). Therefore, to leverage the properties of brain networks in different patterns that nodes in the same functional modules tend to have similar behaviors and clustered representations, we design a orthonormal clustering readout of multiple channels inspired by the reference (Kan et al., 2022b) to take advantage of the modular-level similarities between ROIs in different patterns of brain networks, where nodes in different patterns are assigned softly to well-chosen clusters with an unsupervised process.

Formally, given  $K$  cluster centers where each center has  $V$  dimensions in given channel  $i$ ,  $E_i \in \mathbb{R}^{K \times V}$ , a Softmax projection operator calculates the probability  $P_i^{j,k}$  of assigning node  $j$  to cluster  $k$ :

$$P_i^{j,k} = \frac{\exp\langle Z_i^{L,j}, E_i^k \rangle}{\sum_{k'=1}^K \exp\langle Z_i^{L,j}, E_i^{k'} \rangle} \quad (15)$$

where  $\langle \cdot, \cdot \rangle$  denotes the inner product, and  $Z_i^L$  is the learned set of node embeddings from the last layer of the MHSA module in given channel  $i$ . Using this soft assignment  $P_i \in \mathbb{R}^{N \times K}$  (where  $N$  is the number of nodes), the graph-level embedding  $Z_i^G$  is obtained by:

$$Z_i^G = P_i^\top Z_i^L. \quad (16)$$

To obtain representative soft assignment  $P_i$ , the initialization of cluster centers  $E_i$  is generated by orthonormal initialization (Kan et al., 2022b).

### 3.3.4. Attention-Guided Feature fusion Mechanism for Classification

For the embedding at the graph level  $F_i$  of each channel obtained by flattening  $Z_i^G$  ( $i = 1, 2, 3$ ), we igniting an attention-guided feature fusion mechanism to emphasize discriminative features while suppressing redundant information. The formula can be described as:

$$w_i = \sigma(q_i^T \tanh(W_i Z_i^G)) \quad (17)$$

$$\gamma_i = \frac{\exp^{w_i}}{\exp^{w_1} + \exp^{w_2} + \exp^{w_3}} \quad (18)$$

$$\tilde{F} = \gamma_1 \odot F_1 \parallel \gamma_2 \odot F_2 \parallel \gamma_3 \odot F_3 \quad (19)$$

Table 1: Class distribution of brain network datasets.

Dataset	Class	# Subjects	Disease Type
ADNI	AD	90	Alzheimer’s Disease
	MCI	76	
	NC	96	
TaoWu	PD	20	Parkinson’s Disease
	NC	20	
PPMI	PD	53	Parkinson’s Disease
	prodromal	53	
ABIDE	ASD	488	Autism Spectrum Disorder
	NC	537	

where  $\sigma(\cdot)$  denotes sigmoid function, and  $\odot$  is element-wise multiplication,  $q_i^T$  and  $W_i$  are learnable model parameters. Subsequently, a three-layer multi-layer perceptron (MLP) is employed using  $\tilde{F}$  as input for the prediction head. Finally, the cross-entropy loss function is used as the loss function.

## 4. Experiments

### 4.1. Experimental Settings

#### 4.1.1. Datasets and Preprocessing

To better evaluate the proposed method, we employ four fMRI datasets with varying data sizes. The class distribution of brain network datasets is shown in Table1. 1) **ADNI dataset** (Dadi et al., 2019). The primary goal of ADNI has been to test whether serial magnetic resonance imaging (MRI), positron emission tomography (PET), other biological markers, and clinical and neuropsychological assessment can be combined to measure the progression of mild cognitive impairment (MCI) and early Alzheimer’s disease (AD). The raw images used in this paper were obtained from the Alzheimer’s Disease Neuroimaging Initiative (ADNI) database, which contains 90 Alzheimer’s disease (AD), 96 normal controls (NC) and 76 mild cognitive impairment (MCI). 2) **TaoWu dataset** (Xu et al., 2023). The TaoWu datasets, released by ICI (Xu et al., 2023), is among the earliest image datasets made available for Parkinson’s research, which contains 20 Parkinson’s disease (PD), 20 normal controls (NC). 3) **PPMI dataset** (Xu et al., 2023). The Parkinson’s Progression Markers Initiative (PPMI) is a comprehensive study aiming to identify biological markers associated with Parkinson’s risk, onset, and progression. The raw images used in this article

were obtained from the Parkinson’s progression markers initiative (PPMI) database, which contains 53 Parkinson’s disease (PD) and 53 prodromal. 4) **ABIDE dataset** (Craddock et al., 2013). The Autism Brain Imaging Data Exchange (ABIDE) initiative supports the research on Autism Spectrum Disorder (ASD) by aggregating functional brain imaging data from laboratories worldwide. The raw images used in this article were obtained from the the Autism Brain Imaging Data Exchange (ABIDE) initiative database, which contains 488 Autism spectrum disorder (ASD) patients and 537 normal controls (NC) . We followed in resting-state fMRI data preprocessing (Esteban et al., 2019), which involves a number of pipeline steps, including motion correction, realigning, field unwarping, normalization, bias field correction, and brain extraction. AAL atlas (Tzourio-Mazoyer et al., 2002) is applied to the preprocessed images to parcellate the brain into 90 ROIs, and the BOLD time series of every ROI were obtained by averaging the time series of all voxels inside the ROI.

#### 4.1.2. *Methods for comparison*

The selected baselines correspond to five categories. The first category is traditional machine learning models by the scikit-learn library (Pedregosa et al., 2011) using edge features, including Multilayer Perceptron (MLP) , Support Vector Machine Classifier (SVM), Logistic Regression, and Random Forest. The second category consists of GNNs-based models that learn lower-order topological features from a two-way network. These models include GCN (Kipf and Welling, 2017), GraphSAGE (Hamilton et al., 2017), GAT (Veličković et al., 2018), GroupINN (Yan et al., 2019), BrainGNN (Li et al., 2021), FBNetGen (Kan et al., 2022a), BPI-GNN (Zheng et al., 2024). The third category consists of Transformer-based models that utilize the Transformer architecture to perceive the entire brain picture, including Graph Transformer (Ying et al., 2021), Brain Network Transformer (Kan et al., 2022b), Tsen (Hu et al., 2023), Long-range Brain Transformer (Yu et al., 2024). The fourth category is high-order methods based on hypergraph, including HGCN (Hao et al., 2023), HGAT (Wang et al., 2022). The fifth category is persistent homology (PH)-based models, including Brain-HORS (Santoro et al., 2024), PH-MCI (Bhattacharya et al., 2025), ATPGCN (Bian et al., 2024).

### 4.1.3. Implementation Details

For all experiments, we evaluated the performance in terms of diagnosis accuracy, recall, precision, and F1 score. For dataset partitioning, we adopt an 8:1:1 ratio for training, validation and testing for the ADNI dataset and ABIDE dataset, while using a 3:1:1 ratio for the TaoWu and PPMI datasets. When evaluating model performance, we implement 10-fold cross-validation for the ADNI dataset and ABIDE dataset while 5-fold cross-validation for the others. All models are trained using the Adam optimiser (Kingma and Ba, 2014) with an initial learning rate of  $10^{-4}$  and a weight decay of  $10^{-4}$ , in conjunction with the ReduceLROnPlateau scheduler (Paszke et al., 2017). The batch size is set to 16 for the ADNI dataset and ABIDE dataset while 4 for others, with a maximum number of epochs of 100. After each epoch, the model performance is evaluated using the validation set. We keep the model with the highest F1 score for testing. All experiments are run within the PyTorch framework (Paszke et al., 2017). More details can be described as follows:

- In HOI-Brain, we employ a Julia-based implementation of the Ripserer and PersistenceDiagrams libraries (Bauer, 2021) to compute persistent homology and homological scaffolds, extracting higher-order topological features.
- For traditional machine learning models, the correlation matrix is computed by Pearson correlation for all time series, and its flattened upper triangular matrix is taken as a feature vector. A MLP with three fully connected layers is applied for classification. A SVM with a radial basis function kernel is applied for classification. A LogisticRegression with `solver=lbfgs` is applied for classification. A RandomForest with `n_estimators=300` is applied for classification.
- For GNNs-based models and Transformer-based models, the correlation matrix is calculated using Pearson correlation for all time series. On this basis, the node features in the graph are the columns of the corresponding Pearson correlation matrix. The adjacency matrix in the graph is obtained by thresholding (0.5) the correlation matrix. Generally, two graph convolutional layers and an average pooling layer are used for classification.
- For hypergraph-based high-order methods, specifically, for HGCN, a

graph is first constructed through the correlation matrix, where the correlation of each edge of the graph is greater than 0.7. Each node constructs 2-hyperedges, 3-hyperedges, and 4-hyperedges by selecting its  $k$ -hop neighbors in the graph. For HGAT, the feature of the central node corresponding to each hyperedge is used as the hyperedge feature. When aggregating information, the attention coefficient between the hyperedge and the node is calculated for classification. Note that more HGNNs-based methods applying to brain data have been proposed recently. However, the code of these models is not publicly available, and they require significant engineering which is hard to reproduce fairly based solely on the papers.

- For the persistent homology (PH)-based models, including PH-MCI, ATPGCN. We use the persistent topological features of connected components ( $H0$ ) and loops( $H1$ ) extracting by Ripserer tool. For BrainHORS, following the method, we extract the matrix of violating triangles, the matrix of one-dimensional loops and the matrix of lower-order edge features, then flatten them and feed them into the SVM for classification.

The original codes shared by the authors of these baselines are used for the comparative analysis. We adapt their open-source codes, strictly follow the parameters provided in the papers, and modify them to fit our datasets.

#### 4.2. Model Comparison

Table,2, 3, 4, 5 demonstrate the comparison results on ADNI, TaoWu, PPMI, and ABIDE datasets. The mean and standard deviation of ten-fold cross-validation were listed, with the best results highlighted in bold and the second-best results in underlining. Compared with traditional ML methods, general-purposed GNNs-based models for brain network do not show a significant advantage and attain similar performance in most cases. This finding is consistent with the results reported in existing papers. This is because, under the same input conditions, neural network models typically have a larger number of parameters than conventional machine learning methods when utilizing edge features for better interpretability, making them more susceptible to overfitting. Transformer-based models predominantly outperform GNN-based models across all four datasets in most scenarios, highlighting their superior capability to capture the global structure of brain

Table 2: Performance comparison with five categories of baselines on the ADNI datasets(%). The best results are marked in bold and the second-best results in underlining.

Type	Method	Accuracy	Precision	Recall	F1-score
Traditional Machine Learning Models	MLP	66.3±5.8	67.4±6.4	68.3±6.4	69.1±5.8
	SVM	71.1±5.1	71.6±4.8	71.7±4.8	70.7±5.0
	Logistic Regression	70.7±5.9	73.3±7.7	71.7±7.1	70.5±7.2
	RandomForest	64.8±8.0	66.8±7.2	65.4±8.3	64.9±7.8
GNNs-based models	GCN	60.9±11.8	61.6±12.5	61.1±11.9	60.3±12.1
	GraphSAGE	64.5±8.9	65.6±9.1	64.5±8.9	64.0±9.0
	GAT	60.0±10.1	61.8±10.6	60.0±10.1	59.2±10.3
	GroupINN	57.3±8.8	61.0±9.6	57.4±9.8	56.9±9.1
	FBNETGEN	66.4±7.0	67.7±7.5	67.4±7.1	60.8±5.9
	BPI-GNN	51.4±8.5	49.2±14.6	52.1±8.8	48.0±11.1
Transformer-based models	BrainGNN	58.9±7.7	60.5±8.8	58.9±7.7	58.2±8.0
	Graph Transformer	64.0±6.5	65.6±7.4	64.8±6.5	64.1±6.7
	BrainnetTransformer	69.6±6.2	72.2±6.2	69.5±6.8	69.2±6.3
	LR-BrainTransformer	<u>72.0±8.5</u>	<u>76.5±8.4</u>	<u>72.2±8.0</u>	<u>72.0±9.1</u>
HGNNs-based models	TSEN	62.5±7.3	67.5±8.9	63.2±8.0	62.4±7.4
	HGCN	58.9±7.6	61.2±7.0	60.1±7.7	59.5±7.3
PH-based models	HGAT	54.5±7.5	55.4±7.7	55.3±6.7	54.7±6.9
	PH-MCI	64.8±6.9	67.8±7.3	64.3±5.7	63.5±6.2
	ATPGCN	70.8±6.7	72.6±7.3	70.6±6.3	70.8±6.7
Our Framework	Brain-HORS	64.0±7.2	66.2±7.0	64.0±7.2	64.1±6.8
	HOI-Brain	<b>75.9±8.6</b>	<b>80.0±7.9</b>	<b>75.6±9.1</b>	<b>75.5±9.2</b>

connectomes. HGNNs-based models generally do not demonstrate superiority over other models, with notable performance only observed on the PPMI dataset. This phenomenon can be attributed to two main reasons: first, such models introduce excessive parameters, posing a risk of overfitting; second, their K-hop neighbor-based modeling approach fails to effectively capture the co-fluctuation characteristics among multiple brain regions, thereby inadequately representing high-order interactions. In PH-based models, such as ATPGCN and Brain-HORs, which introduce high-order loops or connected component features extracted via persistent homology for brain disease diagnosis, demonstrate significant superiority compared to both graph neural network (GNN)-based models and traditional machine learning models that rely solely on edge features. This highlights the necessity of incorporating high-order topological features in brain disease diagnosis methods and provides a theoretical foundation for exploring brain diseases from higher-dimensional and more comprehensive perspectives.

Table 3: Performance comparison with five categories of baselines on the TaoWu datasets(%). The best results are marked in bold and the second-best results in underlining.

Type	Method	Accuracy	Precision	Recall	F1-score
Traditional Machine Learning Models	MLP	63.6±15.3	74.4±17.9	65.3±26.7	64.6±15.4
	SVM	57.5±12.8	65.0±22.6	40.0±20.0	46.8±17.1
	Logistic Regression	62.5±23.7	63.7±23.9	60.0±25.5	61.2±24.0
	RandomForest	67.5±16.0	71.3±17.3	70.0±18.7	67.9±11.1
GNNs-based models	GCN	<u>72.5±18.4</u>	72.7±21.7	75.0±25.0	70.6±21.8
	GraphSAGE	67.5±20.3	68.3±21.3	60.0±25.5	63.6±23.5
	GAT	62.5±11.2	63.3±11.3	55.0±18.7	58.1±15.8
	GroupINN	62.5±7.9	59.7±19.0	62.5±7.9	58.5±13.3
	FBNETGEN	57.5±12.8	68.7±26.0	50.0±22.4	52.4±15.4
	BPI-GNN	55.0±12.8	56.7±15.8	55.0±12.8	53.7±12.7
	BrainGNN	60.0±16.6	57.7±19.5	57.6±22.3	60.0±16.6
Transformer-based models	Graph Transformer	67.5±6.1	<u>75.8±6.8</u>	67.5±6.1	64.6±8.1
	BrainnetTransformer	70.0±12.8	72.7±16.7	<b>80.0±24.5</b>	71.9±11.2
	LR-BrainTransformer	65.0±12.2	73.3±9.4	71.2±14.0	<u>74.0±12.1</u>
	TSEN	57.5±10.0	54.3±19.1	57.5±10.0	53.7±13.4
HGNNs-based models	HGCN	55.0±20.3	58.7±23.1	55.0±20.3	52.4±20.2
	HGAT	57.5±15.0	59.0±17.4	57.5±15.0	56.3±15.3
PH-based models	PH-MCI	55.8±6.1	46.8±24.5	60.0±37.4	49.5±25.1
	ATPGCN	57.5±12.8	58.3±12.3	60.0±12.3	58.7±11.5
	Brain-HORS	57.5±20.3	58.3±21.1	57.5±20.3	57.2±20.2
Our Framework	HOI-Brain	<b>77.5±12.3</b>	<b>82.4±9.3</b>	<u>77.5±12.3</u>	<b>75.9±13.9</b>

Our HOI-brain outperforms all 20 baselines on all datasets. In particular, it can be found that the proposed HOI-brain outperforms the traditional machine learning models on all datasets, with average accuracy improved by 12.5 (%), average precision improved by 12.9(%), average recall improved by 14.3(%) and F1-score improved by 12.7(%), respectively. And the proposed HOI-brain outperforms the GNNs-based models on all datasets, with average accuracy improved by 19.6(%), average precision improved by 22.9(%), average recall improved by 19.5(%), and F1-score improved by 19.5(%), respectively. This indicates that our model, by incorporating high-order topological features, is more beneficial for brain disease diagnosis compared to using only low-order edge features. Furthermore, the proposed HOI-Brain outperforms Transformer-based models on all datasets, with average accuracy improved by 13.0(%), average precision improved by 13.4(%), average recall improved by 10.3(%), and F1-score improved by 10.9(%), respectively. This highlights that our model, through the multi-channel brain network trans-

Table 4: Performance comparison with five categories of baselines on the PPMI dataset (%). The best results are marked in bold and the second-best results in underlining.

Type	Method	Accuracy	Precision	Recall	F1-score
Traditional Machine Learning Models	MLP	61.3±5.3	<u>65.3±11.0</u>	54.5±11.4	58.1±6.4
	SVM	<u>64.2±8.3</u>	58.4±10.4	58.4±10.4	61.8±8.7
	Logistic Regression	60.5±7.0	62.4±7.2	54.7±16.8	56.8±11.0
	RandomForest	59.5±5.3	61.7±6.7	56.7±16.3	57.3±7.5
GNNs-based models	GCN	57.5±6.8	58.7±10.1	62.4±5.1	59.6±3.7
	GraphSAGE	60.4±5.6	61.0±8.1	60.6±10.7	60.2±6.5
	GAT	61.3±6.8	61.3±7.3	64.4±8.1	60.4±6.3
	GroupINN	55.6±6.1	55.7±6.2	55.6±6.0	55.4±6.2
	FBNETGEN	59.4±8.4	60.6±10.9	62.4±5.1	60.8±5.9
	BPI-GNN	52.3±14.7	50.5±18.9	49.4±15.1	47.5±14.9
	BrainGNN	60.3±11.3	59.8±11.8	60.5±11.6	60.3±11.3
Transformer-based models	Graph Transformer	59.5±8.5	60.5±8.5	60.0±8.3	58.6±9.2
	BrainnetTransformer	60.4±7.4	65.1±15.9	58.6±15.4	59.1±7.8
	LR-BrainTransformer	58.6±7.0	59.8±10.7	64.4±8.5	60.9±4.7
	TSEN	58.5±7.6	59.3±7.9	58.6±7.5	57.8±7.6
HGNNs-based models	HGCN	64.2±10.0	65.2±10.3	64.3±10.3	<u>63.4±10.5</u>
	HGAT	61.3±5.3	61.9±5.7	61.4±5.4	61.0±5.3
PH-based models	PH-MCI	53.6±4.1	58.8±6.5	60.0±8.4	55.5±6.6
	ATPGCN	61.2±3.5	62.1±3.4	<u>64.5±3.3</u>	62.9±3.3
	Brain-HORS	60.4±7.9	60.8±7.6	60.4±7.9	60.0±8.4
Our Framework	HOI-Brain	<b>66.1±4.0</b>	<b>69.0±4.0</b>	<b>66.3±4.2</b>	<b>64.7±4.7</b>

former, can effectively and holistically integrate complementary information from heterogeneous high-order and low-order topological features while preserving channel-specific properties. Next, when compared to HGNNs-based models, HOI-Brain achieves remarkable improvements with average accuracy improved by 21.8(%), precision improved by 27.0(%), recall improved by 19.4(%), and F1-score improved by 20.5(%). These results clearly demonstrate that our proposed HOI-Brain framework significantly advances the modeling of higher-order interactions through the Multiplication of Temporal Derivatives and the extraction of topological features using persistent homology in brain networks. When specifically compared to Persistent Homology (PH) based models, HOI-Brain achieves significant improvements with average accuracy increased by 17.4(%), precision enhanced by 21.4(%), recall boosted by 14.5(%), and F1-score elevated by 16.2(%). This is partly attributed to our method linking signed HOIs in the brain to higher-order organizations, and partly due to our exploration of more complex signed

Table 5: Performance comparison with five categories of baselines on the ABIDE dataset (%). The best results are marked in bold and the second-best results in underlining.

Type	Method	Accuracy	Precision	Recall	F1-score
Traditional Machine Learning Models	MLP	58.3±6.3	60.3±5.0	59.6±5.4	58.7±6.4
	SVM	61.4±5.5	63.8±5.6	61.4±5.1	62.5±5.0
	Logistic Regression	63.1±5.9	65.5±5.9	63.1±5.3	64.2±5.3
	RandomForest	60.7±5.2	61.0±4.1	<b>68.3±8.4</b>	64.4±5.5
GNNs-based models	GCN	60.4±4.5	61.8±4.3	64.4±7.5	62.9±4.7
	GraphSAGE	61.2±3.6	64.0±4.1	59.3±5.6	61.5±5.5
	GAT	59.3±3.8	57.9±5.3	61.1±3.5	59.5±4.8
	GroupINN	57.1±4.4	58.4±5.0	57.1±4.2	55.7±4.3
	FBNETGEN	58.0±4.2	59.8±4.1	61.1±8.6	60.1±5.2
	BPI-GNN	52.5±4.7	51.7±6.9	54.6±5.5	53.5±4.5
Transformer-based models	BrainnetTransformer	60.5±4.6	59.3±3.9	59.1±5.1	59.8±3.6
	Graph Transformer	57.5±4.2	57.5±4.3	57.3±4.2	57.1±4.2
	LR-BrainTransformer	<u>63.1±4.3</u>	<u>65.5±4.9</u>	63.3±6.0	64.2±4.3
	BrainnetTransformer	63.1±5.8	64.6±5.8	<u>66.1±6.0</u>	<u>65.2±5.2</u>
HGNNs-based models	HGCN	61.0±3.0	55.2±5.3	62.3±4.6	60.4±4.3
	HGAT	58.3±4.3	51.9±5.7	61.4±3.4	59.6±6.3
PH-based models	PH-MCI	57.9±5.2	58.4±4.6	61.5±4.5	59.3±6.2
	ATPGCN	62.2±4.5	62.4±5.3	60.6±5.3	61.8±4.6
	Brain-HORS	63.0±3.4	63.1±3.5	63.4±3.4	62.9±3.5
Our Framework	HOI-Brain	<b>65.6±3.5</b>	<b>66.2±3.8</b>	65.6±3.4	<b>65.3±3.5</b>

quadruplet structures and voids (2D holes) formed by triangular faces and quadruplet.

These experimental results demonstrate the effectiveness of our framework. To the best of our knowledge, our HOI-brain is the first method that distinguishes between positively and negatively synergistic higher-order interactions, and the first attempt to utilize quadruplet-level interaction signatures and two-dimensional void descriptors extracted via Persistent Homology to enhance diagnostic efficacy.

### 4.3. Model analysis

#### 4.3.1. Ablation study

To evaluate the rationality and effectiveness of the proposed model’s architecture, we conducted a series of ablation experiments to assess the impact of different components on overall performance. Our first aim was to evaluate the effectiveness of more complex signed quadriplet structures and voids (2D holes) formed by triangular faces. Specifically, following the method in

Table 6: Performance comparison with varying combinations of features on the ADNI datasets (%). The best results are marked in bold and the second-best results in underlining.

Method	ADNI			
	Accuracy	Precision	Recall	F1-score
edge	68.4±5.5	69.9±5.4	69.3±6.0	68.1±5.7
edge+violating triangles+1D loops	59.7±7.5	61.8±9.5	60.6±7.6	59.0±7.9
edge+violating triangles+good quadruplets	73.9±7.8	74.6±7.2	73.8±8.0	73.7±7.8
edge+1D loops+2D voids	62.9±6.6	68.2±10.2	63.9±6.4	61.7±6.9
edge+good quadruplets+2D voids	<u>74.7±7.4</u>	<u>76.2±7.8</u>	<u>75.5±7.4</u>	<u>74.6±7.6</u>
edge+signed good quadruplets+signed 2D voids	<b>75.9±8.6</b>	<b>80.0±7.9</b>	<b>75.6±9.1</b>	<b>75.5±9.2</b>

Table 7: Performance comparison with varying combinations of features on the ABIDE datasets (%). The best results are marked in bold.

Method	ABIDE			
	Accuracy	Precision	Recall	F1-score
edge	58.3±5.3	58.3±5.4	59.1±4.1	58.1±5.5
edge+violating triangles+1D loops	61.6±4.4	60.0±4.2	63.5±5.9	62.4±4.1
edge+violating triangles+good quadruplets	60.5±4.2	62.4±4.7	59.4±4.3	61.7±4.3
edge+1D loops+2D voids	64.3±3.2	63.3±6.2	60.9±4.7	63.6±5.3
edge+good quadruplets+2D voids	<u>63.7±4.5</u>	<u>63.4±2.5</u>	<u>61.4±4.4</u>	<u>63.5±4.1</u>
edge+signed good quadruplets+signed 2D voids	<b>65.6±3.5</b>	<b>66.2±3.8</b>	<b>65.6±3.4</b>	<b>65.3±3.5</b>

(Santoro et al., 2024), we extract lower-order edge features, violating triangles, one-dimensional loops. In addition, we extract unsigned good quadruplets and unsigned two-dimensional voids based our methods. We implement it within different combinations of these features on all datasets. The experimental results presented in Table 6, 7, A.8, A.9, indicate that integrating both higher-order and lower-order interactions proves to be more effective for brain disorder diagnosis compared to using lower-order interactions alone. Furthermore, quadruplet interactions captured by HOI-Brain have been demonstrated to be more effective in improving diagnosis than triplet interactions. This may be due to the fact that a significant proportion of triplet interactions can be decomposed into a linear combination of pairwise interactions, which is insufficient to capture the true high-order interactions. Additionally, distinguishing between positively and negatively synergistic higher-order interactions to generate signed higher-order structures, as opposed to unsigned ones, can further improve the effectiveness of brain disease diagnosis, which may due to the fact that it can offer detailed

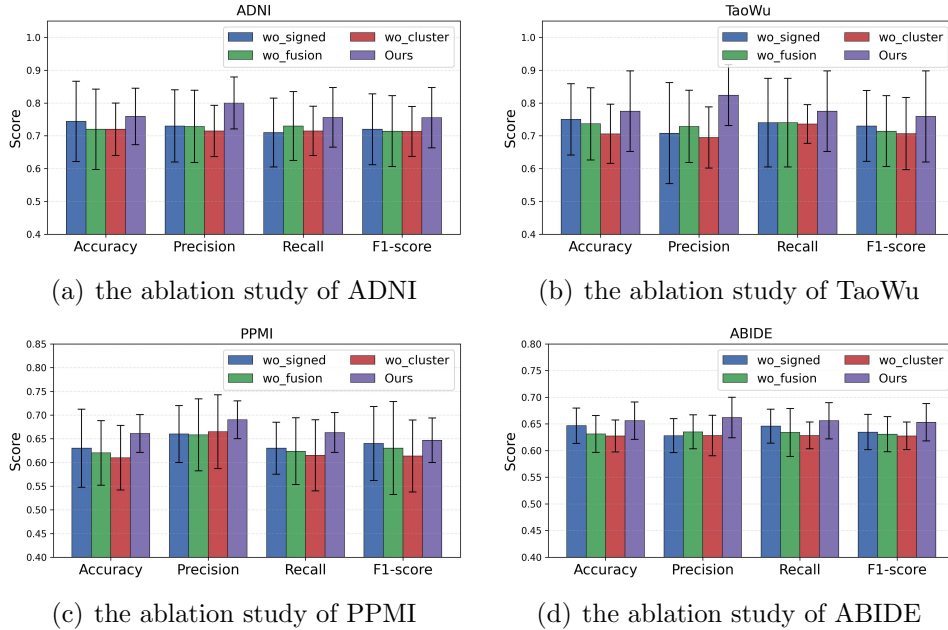


Figure 4: Results of the ablation study in in multi-channel brain network Transformer of HOI-Brain, comparing with three degenerated variants for all datasets.

insights into the communication within the brain.

Our second aim was to evaluate the effectiveness of different components in multi-channel brain network transformer. The different variants are: not adding signed high-order features decoupling mechanism (wo-signed), not adding orthonormal clustering readout of multiple channels, and not adding attention-guided feature fusion mechanism (wo-fusion), and not adding orthonormal clustering readout of multiple channels(wo-cluster). From Fig.4, we can see that adding signed high-order features decoupling mechanism and attention-guided feature fusion mechanism are always helpful as HOI-brain wins all the cases over the variant (wo-signed) or (wo-fusion). This result is consistent with our assumption that, by introducing the attention mechanism, our model can adaptively fuse positive and negative information as well as information from different channels, thereby emphasizing discriminative features while suppressing redundant information. Incorporating orthonormal clustering readout across multiple channels (wo-cluster) is highly beneficial, as this approach effectively captures both low-level and high-level feature patterns, which often reside within distinct functional modular struc-

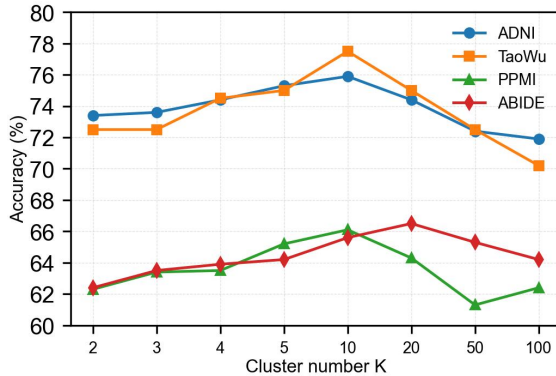


Figure 5: Influence of the key hyper-parameter, the number of clusters, for model performance on accuracy metrics.

tures.

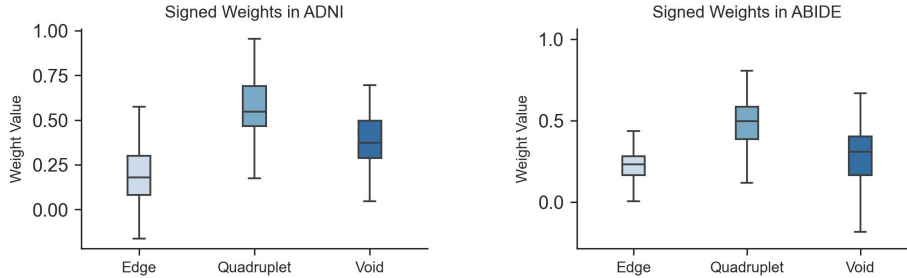
#### 4.3.2. Hyperparameter analysis

To further demonstrate how the design of orthonormal clustering readout across multiple channels affects our model’s performance, we investigate a key hyperparameter: the number of clusters  $K$ . Specifically, we evaluate the method with  $K$  set to 2, 3, 4, 5, 10, 20, 50, and 100. The results of accuracy metric tuning this hyperparameter across all datasets are presented in Fig. 5. The results of other metrics are presented in Fig. B.18. We observe that the model’s performance improves as  $K$  increases from 2 to 10 or 20 but declines when  $K$  rises from 10 or 20 to 100. This suggests that the optimal number of clusters is relatively small, reducing computational cost while aligning with the fact that the typical number of functional modules is fewer than 25, a finding consistent with previous studies (Kan et al., 2022b).

### 4.4. Model Interpretability

#### 4.4.1. In-depth Analysis of Attention Mechanism

To better understand the mechanism of our model, which focuses on the most discriminative information in the brain for the diagnosis of brain diseases, we first performed a visualization analysis of the attention scores  $\gamma_1$ ,  $\gamma_2$  of the attention-guided feature fusion mechanism for all patients of each type of disease, using ADNI and ABIDE as examples. Fig. 6 shows that our model is capable of adaptively learning weights according to the characteristics of different diseases, thereby integrating higher- and lower-order



(a) the attention scores of each channel in ADNI      (b) the attention scores of each channel in ABIDE

Figure 6: The visualization of attention scores for each channel in (a) the ADNI dataset and (b) the ABIDE dataset, as two examples.

topological information for the diagnosis of brain diseases. In addition, we observed that quadruplet-level interaction signatures are significantly more important than two-dimensional void descriptors and edge features, with their average attention scores exceeding 0.5 on both datasets.

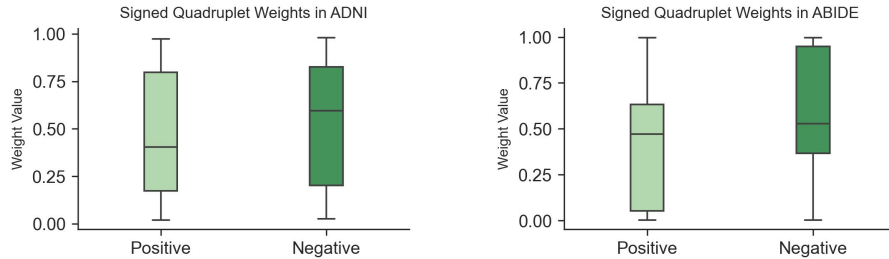
Next, we also conducted a visualization analysis of the attention scores  $\alpha_1$ ,  $\alpha_2$ ,  $\beta_1$ ,  $\beta_2$  derived from the signed high-order feature decoupling mechanism for all patients across each disease type, using ADNI and ABIDE as examples. Fig. 7 shows that across both datasets, the importance of negative synergistic quadruplets is generally greater than that of positive synergistic information in most cases, while the importance of positive synergistic voids exceeds that of negative synergistic information. This new phenomenon may provide a clearer direction for research into the pathological mechanisms of brain diseases.

To further investigate the aforementioned phenomena in the attention mechanism, we conducted inter-group comparisons of the signed high-order topological features, the quadruplet-level interaction signatures and two-dimensional void descriptors, captured by the model in both patient and healthy control groups, using ADNI dataset as example. As shown in Fig. 8, we observed that the group differences in the quadruplet-level interaction signatures were highly significant, with all statistical significance levels at  $p < 0.001$  compared to void descriptors. This finding aligns with the results of our model visualization. This may be because, during disease progression, the direct disruption occurs in the higher-order interactions within the brain, which further affects the high-dimensional hole structures in the brain. More-

over, as the disease progresses, the number of positive quadruplets shows a gradual decreasing trend, while the number of negative quadruplets first decreases and then increases. This indicates that during the transition from CN (cognitively normal) to MCI (mild cognitive impairment), the synergistic interactions in the brain—whether positive or negative—decrease. In contrast, as the condition progresses from MCI to AD (Alzheimer’s disease), brain regions tend to act negative-synergistically and simultaneously reduce their excitability in order to maintain the functionality of various neural modules. Regarding the number of voids, although no clear trend was observed in the progression of the disease, we found that positive voids exhibited more significant intergroup differences compared to negative voids. This further supports the earlier finding that they have higher attention scores. Accordingly, CN tends to utilize positive information to construct the whole-brain topological structure, whereas AD appears to rely more heavily on negative information. These findings may offer a novel perspective on the pathological mechanisms underlying Alzheimer’s disease.

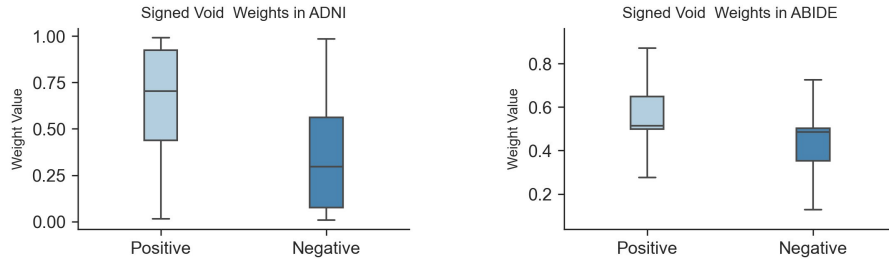
#### 4.4.2. *In-depth Analysis of Cluster Mechanism*

To better understand how our model leverages modular-level similarities between ROIs across different brain network patterns, we first provide a visualization of three attention matrices at the first layer of the multi-head self-attention module on the ADNI and ABIDE datasets in Fig. 9, 10. The attention scores are averaged across all subjects in the ADNI and ABIDE test set. This figure demonstrates that the learned attention scores reveal varying degrees of modularity in both low-order and high-order patterns, highlighting the interpretability of our model. Furthermore, we provide a visualization of three cluster assignment matrices on ADNI and ABIDE dataset in Fig. 11. The cluster assignment matrices are multiplied across layers and averaged across all subjects in the ADNI and ABIDE test set. Each row corresponds to an ROI and each column is a cluster. We observe that the assignment matrix, which is calculated based on the similarity between nodes and clusters, contains only one high-value entry per row in most cases, despite the fact that we did not impose any regularization constraints on the assignment matrix. This indicates that our model can effectively partition nodes into functional modules. Additionally, there are differences between the assignment matrices of low-order and high-order patterns, which further demonstrates that varying degrees of modularity in both low-order and high-order patterns. This result aligns with the visualization of three attention



(a) the attention scores of quadruplet in ADNI

(b) the attention scores of quadruplet in ABIDE



(c) the attention scores of void in ADNI

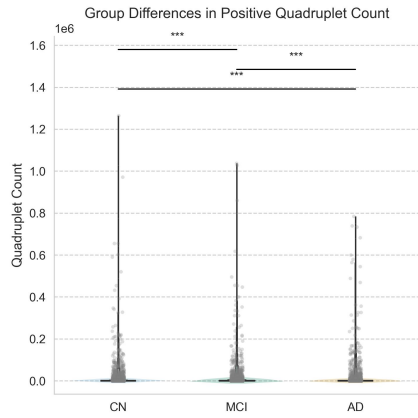
(d) the attention scores of void in ABIDE

Figure 7: The visualization of attention scores for quadruplet in (a) the ADNI dataset and (b) the ABIDE dataset, and the visualization of attention scores for void in (c) the ADNI dataset and (d) the ABIDE dataset

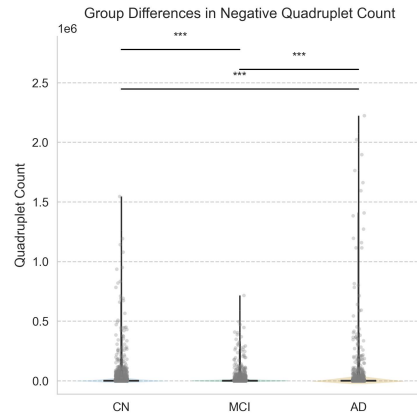
matrices, further indicating the interpretability of our model.

#### 4.4.3. The important brain regions and interactions of brain regions

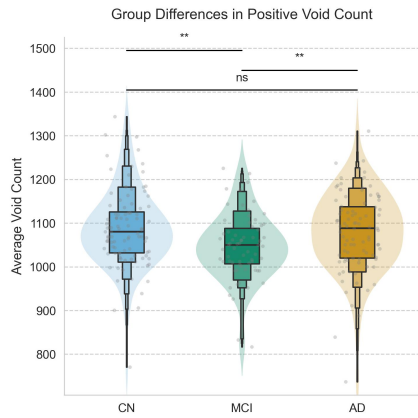
In this section, we further investigate whether the learned ROIs attention scores are interpretable and consistent with previous findings. Here, we take the ADNI, PPMI and ABIDE datasets as examples for discussion of three diseases. These three datasets contain larger sample sizes, enabling the reflection of more generalizable phenomena for brain diseases. First, we analyze the important brain regions and interactions of brain regions associated with brain diseases using HOI-Brain from a more comprehensive perspective rather than a low-level perspective as in previous studies (Kan et al., 2022b; Yu et al., 2024). For each subject, HOI-brain gets three attention matrixes at the first layer of multi-head self attention module. Higher attention scores indicate greater discriminative power of the regions for AD, PD, and



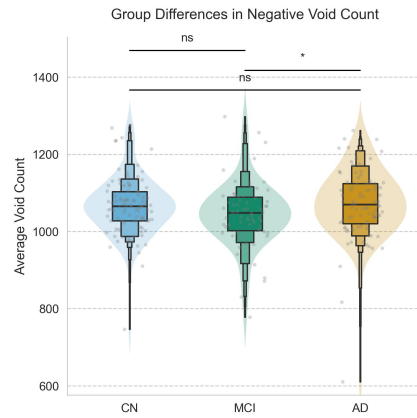
(a) the number of positive quadruplets



(b) the number of negative quadruplets



(c) the number of positive voids



(d) the number of negative voids

Figure 8: Group difference comparison of the signed high-order topological feature quadruplet-level interaction signatures and two-dimensional void descriptors on ADNI. Statistical significance is denoted as follows:  $***p < 0.001$ ,  $**p < 0.01$ ,  $*p < 0.05$ , and  $ns$   $p \geq 0.05$ .”

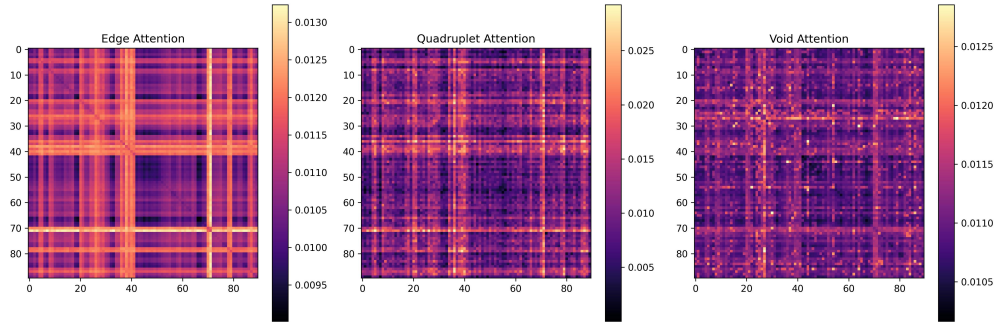


Figure 9: Visualization of three attention matrixes at the first layer of multi-head self-attention module on ADNI.

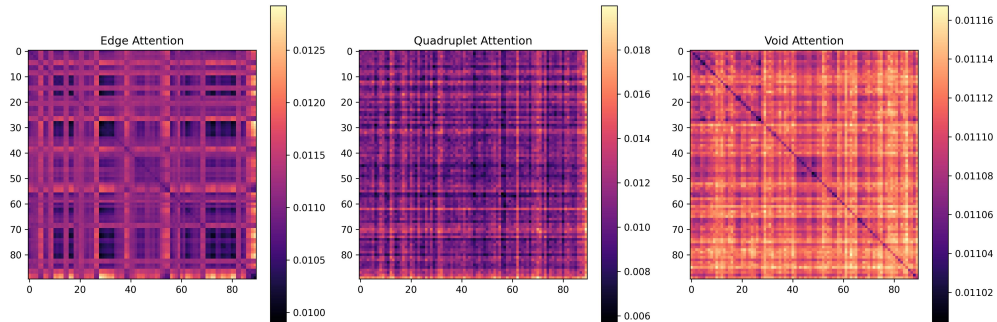
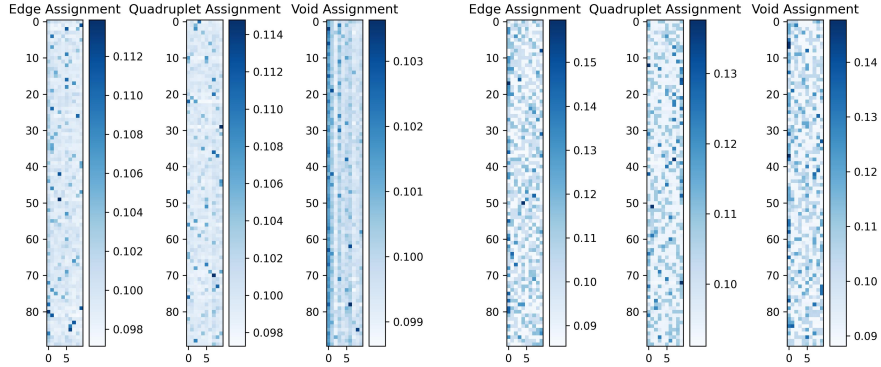


Figure 10: Visualization of three attention matrixes at the first layer of multi-head self-attention module on ABIDE.

ASD. For each disease, we obtain a comprehensive attention matrix that simultaneously captures both low-level and high-level patterns by performing a weighted summation of the three attention matrices for each individual, with the weights derived from the attention scores of each channel. At the regional and regional interaction level, we average the integrated attention matrices across all individuals to derive a matrix representing the importance of interactions between regions. At the regional level, we further compute the row-wise mean of this matrix to obtain the final regional importance scores. We visualize the top ten ROIs and interactions of ROIs with the highest attention scores using BrainNet Viewer (Xia et al., 2013), respectively.

**Alzheimer’s disease (AD).** From the Fig. 12, we observed a significant overlap between the brain regions of interest and those implicated in critical interactions, particularly involving the left caudate nucleus. This may be attributed to the damage sustained by relevant brain regions during



(a) three cluster assignment matrixs on ADNI. (b) three cluster assignment matrixs on ABIDE

Figure 11: Visualization of three cluster assignment matrixs on ADNI and ABIDE datasets

the progression of Alzheimer’s disease, which subsequently leads to weakened connectivity between brain regions. The ten ROIs with the highest attention scores include: Right Caudate (CAU.R), Left Hippocampus (HIP.L), Right Parahippocampal Gyrus (PHG.R), Left Amygdala (AMYG.L), Left Olfactory Cortex (OLF.L), Left Middle Temporal Gyrus (TPOmid.L), Right Olfactory Cortex (OLF.R), Left Parahippocampal Gyrus (PHG.L), Left Caudate (CAU.L), and Right Heschl’s Gyrus (HES.R). These regions are primarily associated with functions such as memory (Hippocampus, Parahippocampal gyrus), emotion (Amygdala), olfaction (Olfactory cortex), motor control (Caudate nucleus), and auditory processing (Heschl’s gyrus). Specifically, the Hippocampus and Parahippocampal gyrus have been widely confirmed to be associated with Alzheimer’s disease (AD) (Bv and Agrawal, 2022; Echávarri et al., 2010), as they are involved in brain memory functions. The Amygdala has also been widely demonstrated to undergo atrophy during the progression of diseases (Zidan et al., 2019). And the Caudate, due to its crucial role in regulating motor control, has significant associations with AD (Zhi et al., 2024). Ye et al. also confirmed the association between the Middle Temporal Gyrus and AD (Ye et al., 2019). The Olfactory Cortex and the Heschl’s Gyrus currently lack direct evidence linking them to Alzheimer’s disease. However, they may be associated with the loss of hearing and smell in Alzheimer’s patients, which suggests that this finding obtained by HOI-brain may provide new insights into the pathology of Alzheimer’s disease. In addition, we observed that most of the top ten ROI interactions with the

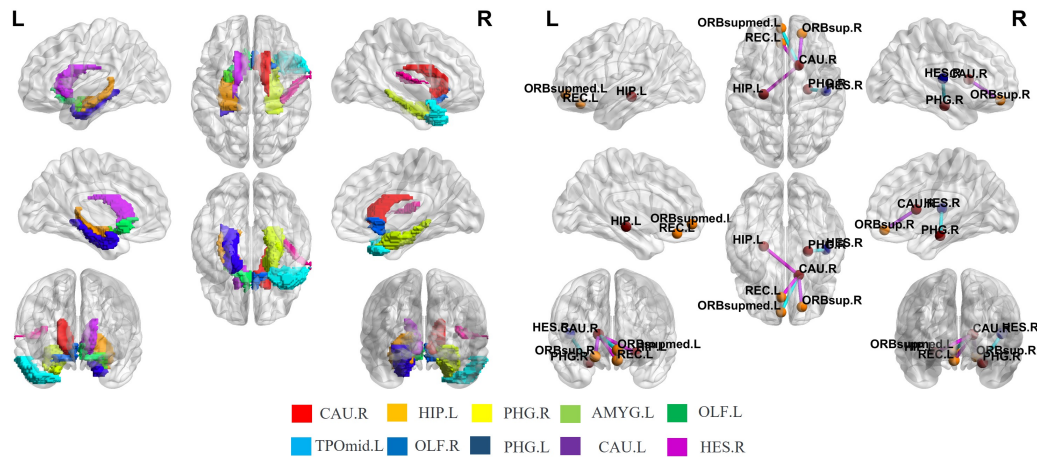


Figure 12: Visualization of top 10 important brain regions(left) and top 10 important interactions of brain regions(right) associated with ADNI.

highest attention scores revolve around the Right Caudate, suggesting that the Right Caudate may serve as a hub node in the brain network and is disrupted during the progression of Alzheimer’s disease, which is consistent with the literature (Zhi et al., 2024).

**Parkinson’s syndrome (PD).** As illustrated in Fig. 13, the ten regions of interest (ROIs) with the highest attention scores are: Right Precentral Gyrus (PCG.R), Left Medial Orbitofrontal Cortex (ORBsupmed.L), Right Inferior Parietal Lobule (IPL.R), Left Amygdala (AMYG.L), Right Triangular Part of the Inferior Frontal Gyrus (IFGtriang.R), Right Superior Parietal Gyrus (SPG.R), Right Inferior Orbitofrontal Cortex (ORBinf.R), Right Thalamus (THA.R), Right Superior Temporal Gyrus (STG.R), and Right Opercular Part of the Inferior Frontal Gyrus (IFGoperc.R). These regions are predominantly implicated in motor execution, reward processing, executive control, affective regulation, and sensorimotor integration—domains known to be disrupted in Parkinson’s disease (PD). Specifically, the Precentral Gyrus (PCG.R), a key component of the primary motor cortex, exhibits marked hypometabolism and altered functional connectivity in PD (Wang et al., 2024b). The left medial orbitofrontal cortex (ORBsupmed.L) is related to decision-making performance in Parkinson’s disease (Kobayakawa et al., 2016). Moreover, compared with healthy controls (HCs), patients with Parkinson’s disease (PD) showed a globally reduced structural - functional connectivity decoupling in The Inferior and Medial Orbitofrontal Cortices (ORBinf.R and

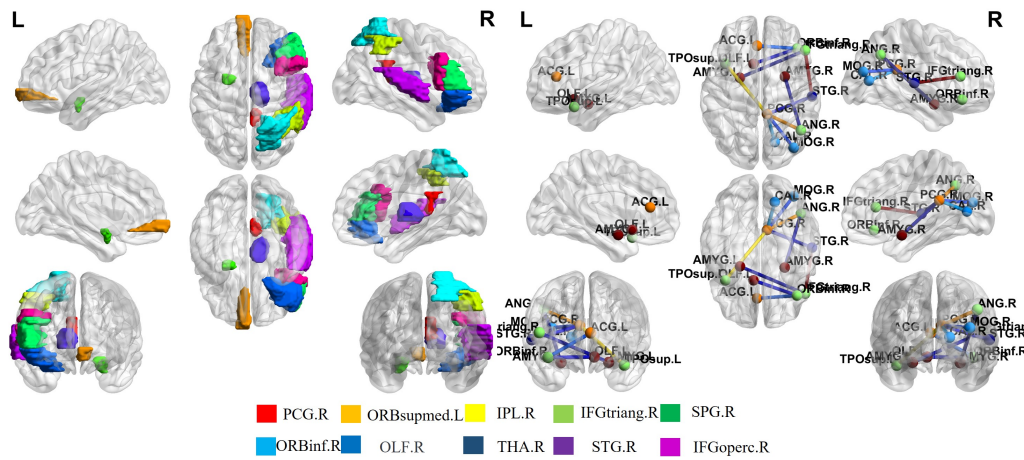


Figure 13: Visualization of top 10 important brain regions(left) and top 10 important interactions of brain regions(right) associated with PPML.

ORBsupmed.L) (Zou et al., 2024). The Amygdala (AMYG.L), central to emotional processing and reward evaluation, demonstrates reduced volume and disrupted connectivity within limbic-striatal circuits in PD, which may underlie affective dysregulation and apathy (Yoshimura et al., 2005). The Thalamus (THA.R), a vital relay hub within cortico-basal ganglia-thalamo-cortical loops, is frequently implicated in PD pathophysiology due to its role in motor and non-motor symptomatology, including tremor and cognitive fluctuations (Zirh et al., 1998). The Triangular and Opercular parts of the Inferior Frontal Gyrus (IFGtriang.R and IFGoperc.R), critical for executive control and language processing, demonstrate impaired activation and connectivity in PD, aligning with cognitive inflexibility and verbal fluency deficits (Li et al., 2020). It is worth noting that although there is currently no direct literature indicating a pathological association between the superior temporal gyrus (STG.R) and Parkinson’s disease, its involvement in auditory processing and social cognition may indirectly contribute to communication difficulties and social withdrawal symptoms in patients with Parkinson’s disease. Crucially, unlike ADNI and ASD, the “core hubs” in the interaction network—PCG.R, STG.R, IFGtriang.R, and ANG.R—did not rank among the top positions in the “key brain importance” list. Conversely, the seven regions listed as “key brain importance,” such as ACG.R, TPOmid.R, and CAU.L, were almost entirely absent from the top 20 strongest interactions. Together, these findings highlight two distinct perspectives on “importance”

in brain: "global centrality" versus "local strong coupling."

**Autism Spectrum Disorder (ASD).** As illustrated in Fig. 13, the ten regions of interest (ROIs) with the highest attention scores are: Right Inferior Temporal Gyrus (ITG.R), Left Supramarginal Gyrus (SMG.L), Left Inferior Temporal Gyrus (ITG.L), Left Triangular Part of the Inferior Frontal Gyrus (IFGtriang.L), Left Caudate (CAU.L), Right Caudate (CAU.R), Left Middle Temporal Gyrus (TPOmid.L), Right Middle Temporal Gyrus (TPOmid.R), Right Anterior Cingulate Gyrus (ACG.R), and Right Rolandic Operculum (ROL.R). These regions are predominantly implicated in social cognition, language processing, executive control, and sensorimotor integration. Specifically, the Inferior Temporal Gyrus (ITG) has been repeatedly reported to exhibit atypical activation and connectivity patterns in individuals with ASD, reflecting its crucial role in face perception and semantic processing (Kim et al., 2021). The Supramarginal Gyrus, a core component of the mirror-neuron system, has also been shown to demonstrate aberrant functional connectivity in ASD, which may contribute to deficits in empathy and social interaction (Bi et al., 2025). The Caudate nucleus, given its involvement in reward processing and cognitive flexibility, has been associated with restricted and repetitive behaviors characteristic of ASD (Adorjan et al., 2017). Furthermore, the Middle Temporal Gyrus and the Anterior Cingulate Gyrus have been implicated in the pathophysiology of ASD through their roles in theory-of-mind and conflict monitoring, respectively (Zhu et al., 2022; Xu et al., 2019). The Rolandic Operculum, although less frequently discussed, is closely linked to auditory and sensorimotor integration, the disruption of which may underlie sensory hypersensitivity commonly observed in ASD (Zhang et al., 2025). Notably, the majority of the top ten ROI interactions with the highest attention scores center on ITG.R, suggesting that this region may also function as a pivotal hub within the brain network and is selectively disrupted during the progression of ASD. This finding aligns with recent literature highlighting the central role of the ITG in the neurodevelopmental trajectory of autism (Kim et al., 2021).

#### *4.4.4. The high-order organization that differ between patients and healthy individuals*

Next, we further investigate whether the higher-order interactions among key brain regions identified by HOI-Brain show significant differences during disease progression, which could offer additional therapeutic insights for brain disease research. For ease of calculation, we selected four out of the

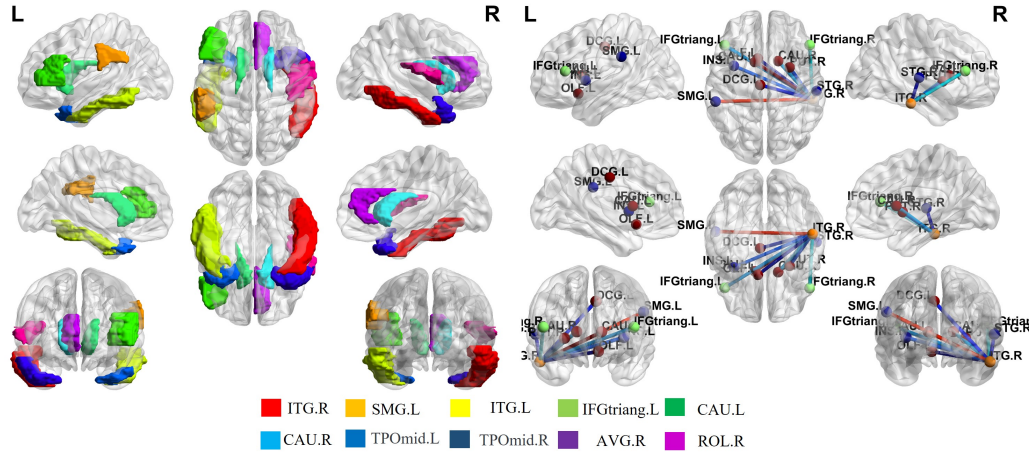


Figure 14: Visualization of top 10 important brain regions(left) and top 10 important interactions of brain regions(right) associated with ABIDE.

top ten key brain regions identified for each disease. Using our proposed time-derivative-multiplication-based co-fluctuation calculation method, we computed the quadruplet interactions among the relevant brain regions and subsequently compared the group differences. As shown in Fig. 15, 16, 17, compared to other brain regions, although these brain regions all demonstrate significant importance in the diagnosis of Alzheimer’s disease (AD) or Autism Spectrum Disorder (ASD)—indicating that they may have sustained varying degrees of damage—their higher-order interactions exhibit notable differences across various stages of disease progression. This suggests a dissociation between higher-order interactions in the brain and the functions of the individual brain regions themselves, which is consistent with the literature (Wang et al., 2019). In addition, we observed that during the transition from healthy individuals to those with Alzheimer’s disease (AD) or autism spectrum disorder (ASD), the positive higher-order interactions between relevant brain regions gradually weaken, indicating a progressive impairment of higher-order synergistic functions among brain regions. On the other hand, the negative higher-order interactions between these brain regions gradually strengthen, reflecting an increasing degree of internal functional disruption in the brain. This phenomenon is consistent with findings reported in previous literature (Santoro et al., 2024). However, this phenomenon is exactly the opposite in Parkinson’s syndrome, which may be due to the fact that Parkinson’s patients, because of their motor impairments, are prone to hallu-

cinations. Hallucinations in Parkinson’s syndrome may result from excessive influence of higher-order brain regions on early sensory processing, which is consistent with the enhanced functional integration between sensory and higher-order networks (Tan et al., 2023).

**Alzheimer’s disease (AD).** As shown in Fig. 15, in particular, the quadruplet interactions among CAU.R, HIP.L, PHG.R, and AMYG.L; the quadruplet interactions among OLF.L, HIP.L, PHG.R, and AMYG.L; and the quadruplet interactions among CAU.R, OLF.L, PHG.R, and AMYG.L, which involve the cortico-striatal-olfactory circuit, exhibit significant inter-group differences during the progression from cognitively normal (CN) to mild cognitive impairment (MCI), with  $p$ -values  $< 0.05$ . However, these differences become less pronounced during the progression from MCI to AD, with  $p$ -values  $\geq 0.05$ . This suggests that these higher-order interactions may serve as potential biomarkers for the early diagnosis of Alzheimer’s disease. In contrast, the quadruplet interactions among CAU.R, TPOmid.L, HIP.L, and AMYG.L, which involves the ‘social-reward-emotion-memory’ integrated circuit, shows a significant inter-group differences throughout the entire AD progression, with  $p$ -values  $< 0.001$ . This indicates that these higher-order interactions may be persistently disrupted across the entire disease course, playing a critical role in AD pathogenesis.

**Parkinson’s syndrome (PD).** As shown in Fig. 16, the quadruplet interactions among PCG.R, ORBsupmed.L, IPL.R, and SPG.R; the interactions among PCG.R, ORBsupmed.L, IPL.R, and IFGoperc.R; and those among PCG.R, ORBsupmed.L, IPL.R, and STG.R, which collectively engage the dorsal attention network (DAN) and fronto-parietal executive control circuits, exhibit significant inter-group differences ( $p < 0.05$ ) between healthy controls and early-stage PD patients. These findings suggest that these functional connectivity patterns may serve as potential early biomarkers for cognitive-motor integration deficits characteristic of the prodromal stages of PD. In addition, the quadruplet interactions involving PCG.R, ORBsupmed.L, THA.R, and IFGoperc.R, which map onto the mesocortical limbic-striatal-thalamic loop, show inter-group differences ( $p < 0.001$ ). This persistent disruption aligns with the progressive degeneration of dopaminergic pathways and thalamocortical relay integrity, implicating these interactions in both motor dysfunction (e.g., bradykinesia) and non-motor symptoms (e.g., apathy, executive decline) throughout PD pathogenesis. critical role in PD-related motor and cognitive dysfunction.

**Autism Spectrum Disorder (ASD).** From Fig. 17, we observed that

the quadruplet interactions among the top five key brain regions—including the interactions between ITG.R, SMG.L, ITG.L, and IFGtriang.L; between SMG.L, ITG.L, IFGtriang.L, and CAU.L; between ITG.R, ITG.L, IFGtriang.L, and CAU.L; between ITG.R, SMG.L, IFGtriang.L, and CAU.L; and between ITG.R, SMG.L, ITG.L, and CAU.L, which involves a "visual-auditory-semantic-action-control" closed-loop system. These interactions exhibited significant inter-group differences throughout the entire progression of Autism Spectrum Disorder (ASD). Such quadruplet interactions may serve as potential biomarkers for investigating tool-use deficits, semantic control impairments, and action-language disconnection in social communication associated with autism. However, the quadruplet interactions among ITG.L, IFGtriang.L, CAU.L, and CAU.R show no significant inter-group differences throughout the entire AD progression, with p-values  $\geq 0.05$ . This suggests a dissociation between higher-order brain interactions and the functions of individual brain regions themselves.

## 5. Discussion

### 5.1. The model

The recent conceptual and technical advances in fMRI data analysis provide an opportunity for the field to not only the effectiveness of brain disease diagnosis deepen our understanding of brain disease mechanisms but also deepen our understanding of brain disease mechanisms (Zheng et al., 2024; Luo et al., 2025; Kan et al., 2022b; Yu et al., 2024; Wang et al., 2022; Hao et al., 2023; Bian et al., 2024; Bhattacharya et al., 2025). However, current methods overlook more higher-order patterns with signs, limiting an integrated understanding of brain-wide communication for brain disease diagnosis.

In this study, we focused on the importance of signed higher-order(group) interactions in fMRI signals, which were inferred using a recently developed topological approach (Hyekyoung et al., 2011). Our proposed HOI-Brain incorporates: (i) a novel higher-order interaction representation strategy via Multiplication of Temporal Derivatives (MTD) to quantify dynamic functional co-fluctuations of group ROIs; (ii) a novel high-order feature extraction method that links higher-order interactions (HOIs) in the brain to higher-order organizational structures, focusing on quadruplet-level interaction signatures and two-dimensional void descriptors extracted through Persistent

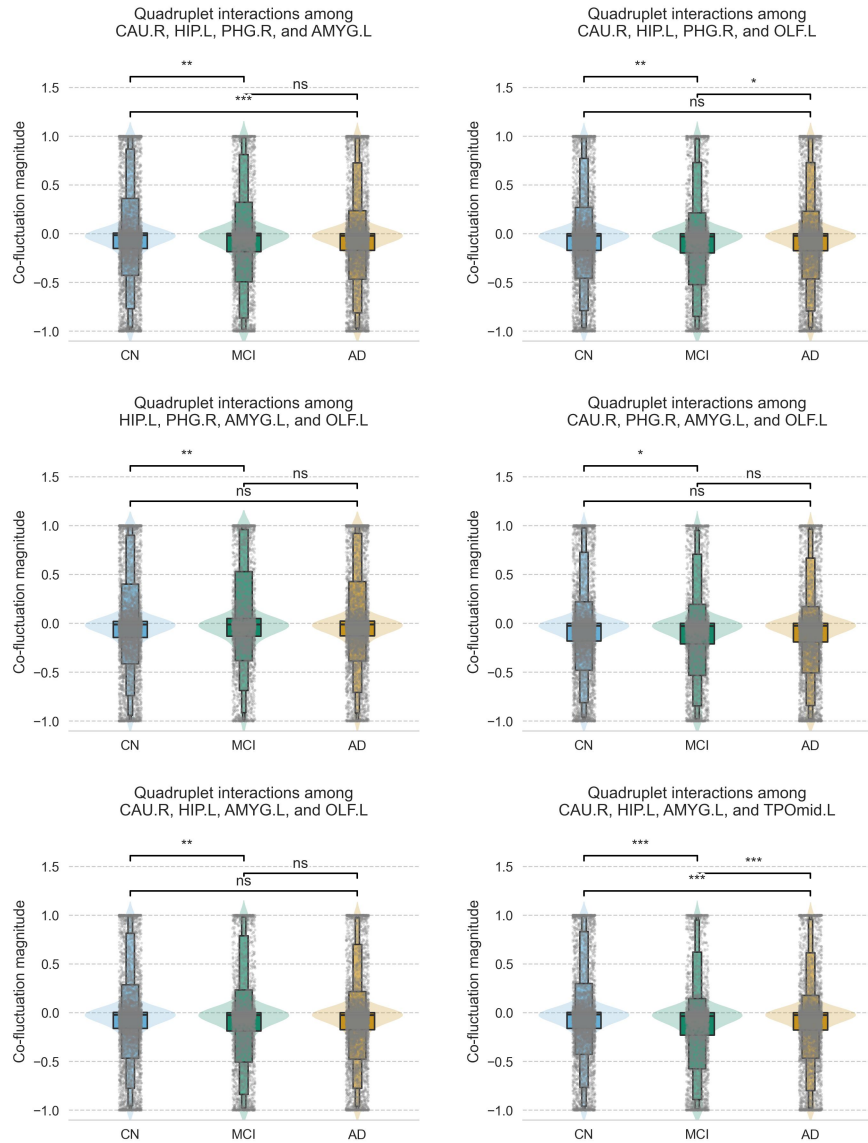


Figure 15: Group difference comparison of quadruplet interactions among the relevant brain regions (CAU.R, HIP.L, PHG.R, AMYG.L, OLF.L, TPOMid.L) on ADNI. Statistical significance is denoted as follows: \*\*\* $p < 0.001$ , \*\* $p < 0.01$ , \* $p < 0.05$ , and ns  $p \geq 0.05$ .”

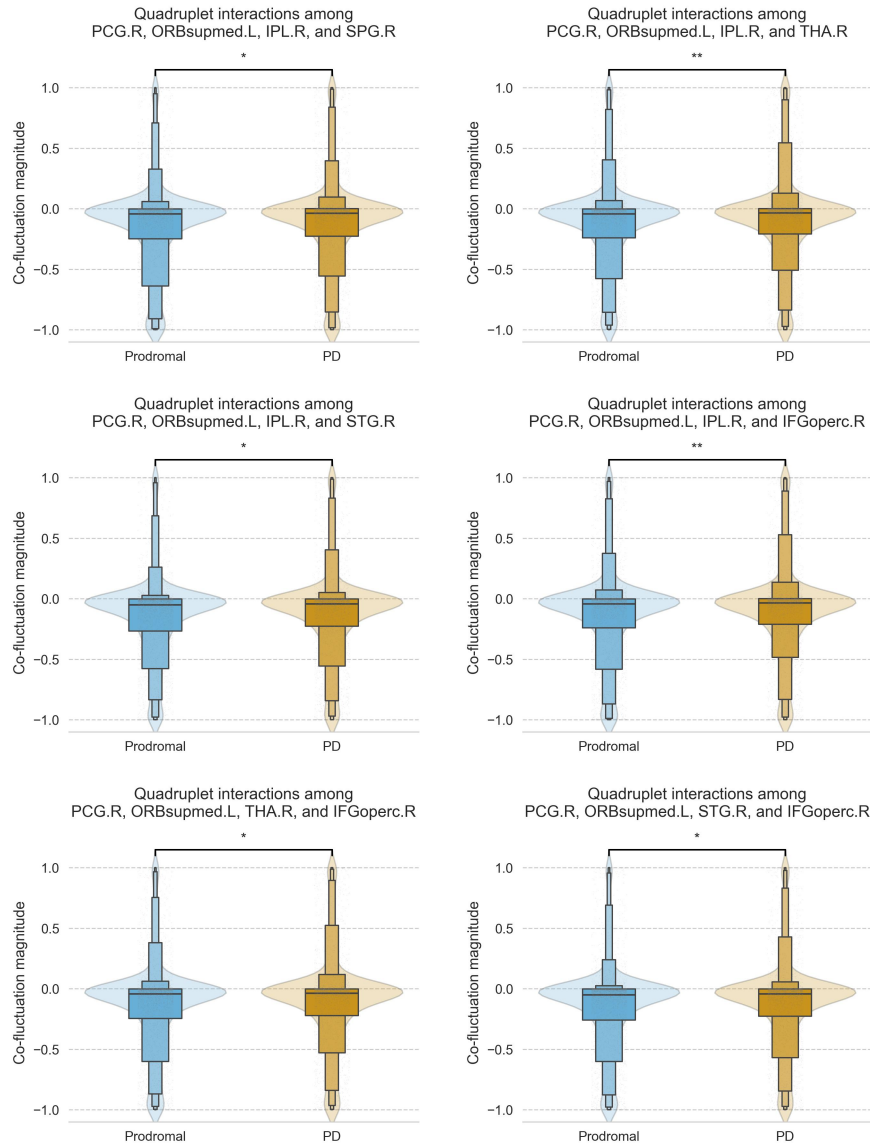


Figure 16: Group difference comparison of quadruplet interactions among the relevant brain regions (PCG.R, ORBsupmed.L, IPL.R, SPG.R, THA.R, STG.R, IPL.R, IFGoperc.R) on PPMI. Statistical significance is denoted as follows: \*\*\* $p < 0.001$ , \*\* $p < 0.01$ , \* $p < 0.05$ , and ns  $p \geq 0.05$ .

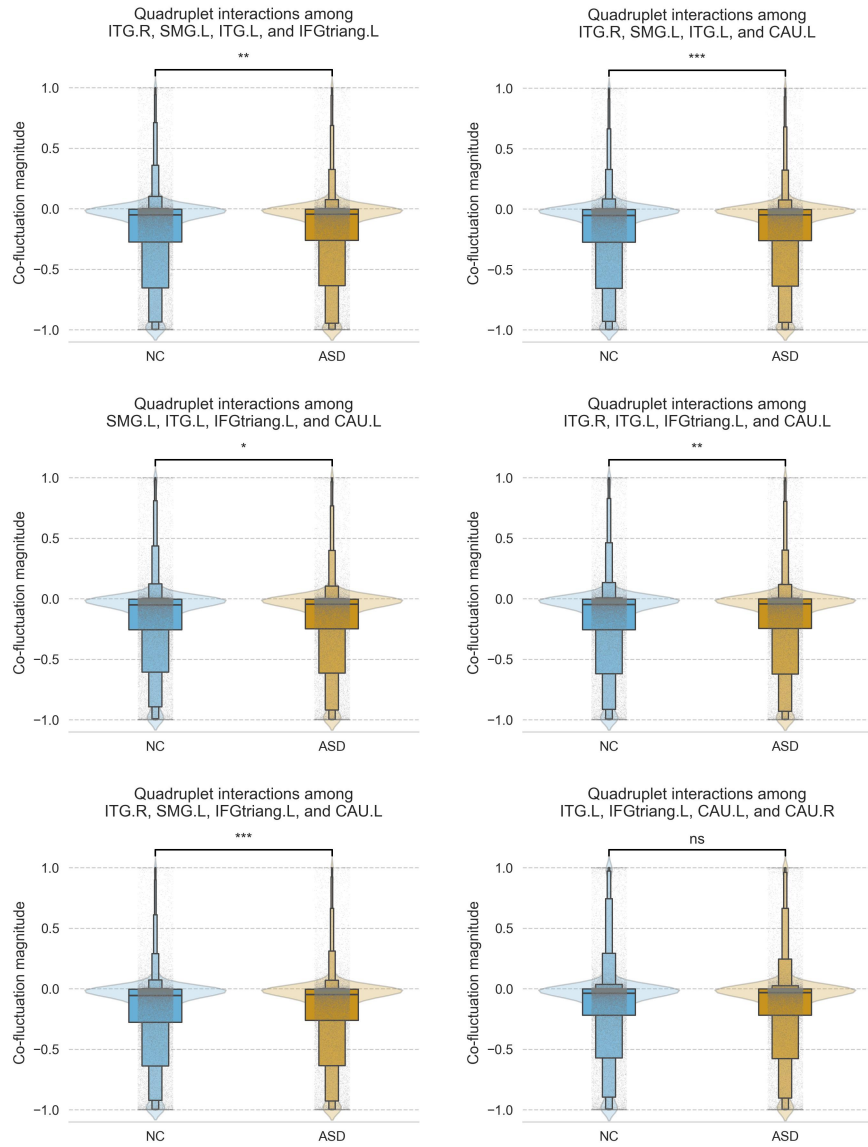


Figure 17: Group difference comparison of quadruplet interactions among the relevant brain regions (ITG.R, SMG.L, ITG.L, IFGtriang.L, CAU.L, and CAU.R) on ABIDE. Statistical significance is denoted as follows: \*\*\* $p < 0.001$ , \*\* $p < 0.01$ , \* $p < 0.05$ , and ns  $p \geq 0.05$ .”

Homology; (iii) a pioneering effort to distinguish between positively and negatively synergistic higher-order interactions in the brain; (iv) a novel multi-channel brain network Transformer that integrates lower-order edge features with higher-order topological invariants. This new framework emphasizes the potential of quadruplet or higher-order region interactions—representing critical advancements for precision medicine, a deeper understanding of neurological disorders, and broader contributions to neuroimaging research. It demonstrates superior prediction accuracy for classifying Alzheimer’s Disease (AD), Parkinson’s Disease (PD), and Autism Spectrum Disorder (ASD) compared to traditional machine learning models, graph neural network (GNN)-based models, transformer-based models, hypergraph neural network (HGNN)-based models, and the Persistent Homology (PH)-based models. And ablation study also indicates that the effectiveness of quadruplet interactions compared to triplet interactions, the effectiveness of distinguishing between positively and negatively synergistic higher-order interactions, and the effectiveness of different components in model.

Our investigations revealed intriguing patterns. When designing an orthonormal clustering readout to identify clusters of functionally similar nodes through soft clustering with orthonormal constraints, we found that assigning nodes from different modes to distinct functional modules significantly improves classification accuracy. This suggests that both low-level and high-level feature patterns—often residing within distinct functional modular structures—play a critical role. This phenomenon is consistent with findings reported in previous literature (Wang et al., 2019). This new discovery also provides a new opportunity for brain disease diagnostic models—specifically, how to effectively identify and integrate low-order and high-order patterns across different functional modules in the brain.

In addition, our investigation into the most discriminative neural patterns using attention mechanism revealed that quadruplet-level interaction signatures exhibit substantially greater importance than two-dimensional void descriptors and edge features in both the ADNI and ABIDE datasets. Notably, negative synergistic quadruplets generally demonstrate higher importance than their positive synergistic quadruplets, whereas positive synergistic voids surpass negative synergistic voids in significance. This novel observation may offer critical insights into the pathological mechanisms underlying brain disorders. To further validate these findings, we performed inter-group comparisons of signed high-order topological signatures in the ADNI dataset. The results revealed highly significant group differences in the number of

quadruplet-level interaction signatures (all  $p < 0.001$ ) compared to void descriptors). Moreover, positive voids exhibited more pronounced inter-group differences than negative voids. These findings suggest that disease progression may primarily disrupt higher-order neural interactions, which subsequently influence high-dimensional hole structures. An intriguing pattern emerged in the comparative analysis of cognitively normal (CN) individuals and those with Alzheimer’s disease (AD). CN individuals appear to rely more on positive information for whole-brain topological organization, whereas AD patients show a greater dependence on negative information. Furthermore, longitudinal trends indicate that the number of positive quadruplets gradually declines with disease progression, while negative quadruplets follow a biphasic trajectory—decreasing initially and then increasing. This implies that during the transition from CN to mild cognitive impairment (MCI), both positive and negative synergistic interactions diminish. However, as the condition advances from MCI to AD, neural networks increasingly adopt negative synergy while suppressing excitability, possibly as a compensatory mechanism to preserve functional integrity across neural modules.

When exploring the important brain regions and their interactions associated with brain diseases, we use HOI-Brain to identify them from a more comprehensive perspective, rather than the low-level perspective adopted in previous studies (Yan et al., 2019; Li et al., 2021). These findings, serving as potential biomarkers, are consistent with a large body of existing literature reports (Zidan et al., 2019; Zhi et al., 2024; Ye et al., 2019; Kim et al., 2021), and also provide new insights for brain disease diagnosis. Specifically, the right caudate may serve as a hub node within the brain network and exhibits disruptions during the progression of Alzheimer’s disease, which is consistent with previous literature (Zhi et al., 2024). Similarly, the right inferior temporal gyrus (ITG.R) appears to function as another pivotal hub within the brain network and is selectively disrupted during the progression of Autism Spectrum Disorder (ASD) (Kim et al., 2021).

Furthermore, the high-order organizational patterns identified by HOI-Brain offer novel insights into the diagnosis of brain diseases. Specifically, the quadruplet interactions among CAU.R, HIP.L, PHG.R, and AMYG.L; the quadruplet interactions among OLF.L, HIP.L, PHG.R, and AMYG.L; and the quadruplet interactions among CAU.R, OLF.L, PHG.R, and AMYG.L, which involve the cortico-striatal-olfactory circuit, may serve as potential biomarkers for the early diagnosis of Alzheimer’s disease with p-values  $< 0.05$  during the progression from cognitively normal (CN) to mild cognitive im-

pairment (MCI). Notably, although these brain regions identified by HOI-Brain demonstrate significant importance in the diagnosis of Alzheimer’s disease (AD) or Autism Spectrum Disorder (ASD) indicating that they may have sustained varying degrees of damage; however, their higher-order interactions exhibit notable differences across various stages of disease progression. This suggests a dissociation between higher-order interactions in the brain and the functions of the individual brain regions themselves, which is consistent with the previous studies (Wang et al., 2019). In addition, we observed that during the transition from healthy individuals to those with Alzheimer’s disease (AD) or autism spectrum disorder (ASD), the positive higher-order interactions between relevant brain regions gradually weaken, indicating a progressive impairment of higher-order synergistic functions among brain regions. On the other hand, the negative higher-order interactions between these brain regions gradually strengthen, reflecting an increasing degree of internal functional disruption in the brain. This phenomenon is consistent with findings reported in previous literature (Santoro et al., 2024). However, this phenomenon is exactly the opposite in Parkinson’s syndrome, which may be due to the fact that Parkinson’s patients, because of their motor impairments, are prone to hallucinations. Hallucinations in Parkinson’s syndrome may result from excessive influence of higher-order brain regions on early sensory processing, which is consistent with the enhanced functional integration between sensory and higher-order networks (Tan et al., 2023).

### *5.2. Limitation and future work*

We acknowledge several limitations of our study, which also serve as inspiration for future research: **1) Ignored the discordant signs of negative:** In this paper, we focus solely on the concordant signs of positive effects, while only exploring the influence of discordant signs of negative within the interpretable section. These discordant signs are known to play a critical role in the overall system dynamics, as they may reflect redundant or conflicting information across multiple brain regions. Future work should investigate alternative methods to more explicitly address decoherent patterns in the data. **2) Lack of dynamic exploring for higher-order topological features:** To mitigate noise in fMRI data, we analyze average statistics across multiple time frames, which helps extract stable low-order and high-order patterns. However, our current approach does not account for the temporal dependencies in higher-order topological features—i.e., how prior time points influence subsequent ones. Since our model reveals that these high-order pat-

terns evolve dynamically over time, further investigation into this temporal evolution could provide novel insights into disease progression. This opens up promising avenues for modeling the dynamic nature of brain network topology. **3) Limited modality of experimental data:** Currently, our analysis is based solely on fMRI data. While these data effectively demonstrate the importance of higher-order interactions in brain network analysis, other time-series modalities—such as EEG or MEG—remain unexplored. In future work, we plan to extend our framework to multimodal neuroimaging data and develop methods tailored to capturing higher-order interactions across different temporal scales.

## 6. Conclusions

In summary, we propose a new framework, HOI-Brain (Higher-Order Interactions in Brain Network), which can accurately capture signed higher-order interactions in brain networks, extract interpretable signed higher-order topological features, and further exploit the information between lower-order and higher-order features for brain disorder diagnosis. We applied BrainGNN to datasets for Alzheimer’s disease, Parkinson’s syndrome, and autism. With the powerful interpretability, HOI-brain not only performs better on classification than 20 baselines, but also detects salient brain regions associated with classification and discovers important higher-order organizations. Overall, our model shows superiority over alternative graph learning and traditional machine learning classification models. By investigating By analyzing the attention maps of our multi-channel brain transformer, our study identifies salient regions of interest (ROIs) and their key interactions—from a whole-brain perspective—to distinguish brain disorders from healthy controls. Additionally, we uncover higher-order organizational patterns associated with specific disease progression stages. Notably, our framework is generalizable to the analysis of other neuroimaging time-series data. Our proposed framework demonstrates the potential of quadruplet or higher-order region interactions—critical advancements for precision medicine, enhanced understanding of neurological disorders, and broader contributions to neuroimaging research.

## 7. Declaration of Competing Interest

The authors declare that they have no known competing financial interests or personal relationships that could have appeared to influence the work

reported in this paper.

## 8. Acknowledgements

This work was supported in part by the National Natural Science Foundation of China No.12471330 and the National Natural Science Foundation of China No.12231018.

## References

- Adorjan, I., Ahmed, B., Feher, V., Torso, M., Krug, K., Esiri, M., Chance, S., Szele, F., 2017. Calretinin interneuron density in the caudate nucleus is lower in autism spectrum disorder. *Brain* 140.
- Barrat, A., Barthelemy, M., Pastor-Satorras, R., Vespignani, A., 2004. The architecture of complex weighted networks. *Proceedings of the National Academy of Sciences of the United States of America* 101, 3747–52.
- Battiston, F., Cencetti, G., Iacopini, I., Latora, V., Lucas, M., Patania, A., Young, J.G., Petri, G., 2020. Networks beyond pairwise interactions: Structure and dynamics. *Physics Reports* 874, 1–92. Networks beyond pairwise interactions: Structure and dynamics.
- Bauer, U., 2021. Ripser: efficient computation of vietoris–rips persistence barcodes. *Journal of Applied and Computational Topology* 5.
- Bhattacharya, D., Kaur, R., Aithal, N., Sinha, N., Gregor Issac, T., 2025. Persistent homology for mci classification: a comparative analysis between graph and vietoris-rips filtrations. *Frontiers in Neuroscience* Volume 19 - 2025.
- Bi, F., Jia, Z., Lv, L., Zhang, Y., Zhu, C., Wan, C., 2025. Analysis of brain functional connectivity in children with autism spectrum disorder and sleep disorders: a fnirs observational study. *Frontiers in Psychology* 16.
- Bian, C., Xia, N., Xie, A., Cong, S., Dong, Q., 2023. Adversarially trained persistent homology based graph convolutional network for disease identification using brain connectivity. *IEEE transactions on medical imaging* PP.

- Bian, C., Xia, N., Xie, A., Cong, S., Dong, Q., 2024. Adversarially trained persistent homology based graph convolutional network for disease identification using brain connectivity. *IEEE Transactions on Medical Imaging* 43, 503–516.
- Bullmore, E., Sporns, O., 2009. Complex brain networks: Graph theoretical analysis of structural and functional systems. *Nature reviews. Neuroscience* 10, 186–98.
- Bv, M., Agrawal, A., 2022. Hippocampus and its involvement in alzheimer’s disease: a review. *3 Biotech* 12.
- Cassidy, B., Bowman, F.D., Rae, C., Solo, V., 2018. On the reliability of individual brain activity networks. *IEEE Transactions on Medical Imaging* 37, 649–662.
- Chelaru, M., Eagleman, S., Andrei, A., Milton, R., Kharas, N., Dragoi, V., 2021. High-order interactions explain the collective behavior of cortical populations in executive but not sensory areas. *Neuron* 109.
- Craddock, C., Benhajali, Y., Carlton, C., Francois, C., Evans, A., Jakab, A., Khundrakpam, B., Lewis, J., Qingyang, I., Michael, M., Chaogan, Y., Bellec, P., 2013. The neuro bureau preprocessing initiative: open sharing of preprocessed neuroimaging data and derivatives. *Frontiers in Neuroinformatics* 7.
- Dadi, K., Rahim, M., Abraham, A., Chyzhyk, D., Milham, M., Thirion, B., Varoquaux, G., 2019. Benchmarking functional connectome-based predictive models for resting-state fmri. *NeuroImage* 192.
- Delabays, R., De Pasquale, G., Dörfler, F., Zhang, Y., 2025. Hypergraph reconstruction from dynamics. *Nature Communications* 16.
- Echávarri, C., Aalten, P., Uylings, H., Jacobs, H., Visser, P., Gronenschild, E., Verhey, F., Burgmans, S., 2010. Atrophy in the parahippocampal gyrus as an early biomarker of alzheimer’s disease. *Brain structure & function* 215, 265–71.
- Esteban, O., Markiewicz, C.J., Blair, R.W., Moodie, C.A., Isik, A.I., Erramuzpe, A., Kent, J.D., Goncalves, M., DuPre, E., Snyder, M., Oya, H., Ghosh, S.S., Wright, J., Durnez, J., Poldrack, R.A., Gorgolewski, K.J.,

2019. fmriprep: a robust preprocessing pipeline for functional mri. *Nature methods* 16, 111—116.
- Faskowitz, J., Esfahlani, F., Jo, Y., Sporns, O., Betzel, R., 2020. Edge-centric functional network representations of human cerebral cortex reveal overlapping system-level architecture. *Nature Neuroscience* 23, 1–11.
- Fornito, A., Zalesky, A., Bullmore, E., 2016. *Fundamentals of Brain Network Analysis*. 1 ed., Academic Press, United States of America.
- Fotiadis, P., Parkes, L., Davis, K., Satterthwaite, T., Shinohara, R., Bassett, D., 2024. Structure–function coupling in macroscale human brain networks. *Nature Reviews Neuroscience* 25.
- Hamilton, W., Ying, Z., Leskovec, J., 2017. Inductive representation learning on large graphs, in: Guyon, I., Luxburg, U.V., Bengio, S., Wallach, H., Fergus, R., Vishwanathan, S., Garnett, R. (Eds.), *Advances in Neural Information Processing Systems*, Curran Associates, Inc.
- Hao, X., Li, J., Ma, M., Qin, J., Zhang, D., Liu, F., 2023. Hypergraph convolutional network for longitudinal data analysis in alzheimer’s disease. *Computers in Biology and Medicine* 168, 107765.
- Hu, J., Huang, Y., Dong, S., 2023. Transformer and snowball graph convolution learning for brain functional network analysis, in: *2023 IEEE International Conference on Bioinformatics and Biomedicine (BIBM)*, pp. 2809–2816.
- Hyekyoung, L., Chung, M., Kang, H., Kim, B., Lee, D., 2011. Discriminative persistent homology of brain networks. *Proceedings - International Symposium on Biomedical Imaging* , 841–844.
- Jie, B., Wee, C.Y., Shen, D., Zhang, D., 2016. Hyper-connectivity of functional networks for brain disease diagnosis. *Medical image analysis* 32, 84—100. doi:10.1016/j.media.2016.03.003.
- Kan, X., Cui, H., Lukemire, J., Guo, Y., Yang, C., 2022a. Fbnetgen: Task-aware gnn-based fmri analysis via functional brain network generation. *Proceedings of machine learning research* 172, 618—637.

- Kan, X., Dai, W., Cui, H., Zhang, Z., Guo, Y., Yang, C., 2022b. Brain network transformer, in: Koyejo, S., Mohamed, S., Agarwal, A., Belgrave, D., Cho, K., Oh, A. (Eds.), *Advances in Neural Information Processing Systems*, Curran Associates, Inc.. pp. 25586–25599.
- Kim, D., Lee, J., Jeong, B., Ahn, J., Kim, J., Lee, E., Kim, H., Lee, H.j., Han, C., 2021. Overconnectivity of the right heschl’s and inferior temporal gyrus correlates with symptom severity in preschoolers with autism spectrum disorder. *Autism Research* 14, 2314–2329.
- Kim, S., Lee, S.Y., Gao, Y., Antelmi, A., Polato, M., Shin, K., 2024. A survey on hypergraph neural networks: An in-depth and step-by-step guide, in: *Proceedings of the 30th ACM SIGKDD Conference on Knowledge Discovery and Data Mining*, Association for Computing Machinery, New York, NY, USA. p. 6534–6544.
- Kingma, D., Ba, J., 2014. Adam: A method for stochastic optimization. *International Conference on Learning Representations* .
- Kipf, T.N., Welling, M., 2017. Semi-supervised classification with graph convolutional networks, in: *International Conference on Learning Representations*.
- Kobayakawa, M., Tsuruya, N., Kawamura, M., 2016. Decision-making performance in parkinson’s disease correlates with lateral orbitofrontal volume. *Journal of the Neurological Sciences* 372.
- Li, M.g., Liu, T.f., Zhang, T.h., Chen, Z.y., Nie, B.b., Lou, X., Wang, Z.f., Ma, L., 2020. Alterations of regional homogeneity in parkinson’s disease with mild cognitive impairment: a preliminary resting-state fmri study. *Neuroradiology* 62.
- Li, X., Zhou, Y., Dvornek, N., Zhang, M., Gao, S., Zhuang, J., Scheinost, D., Staib, L., Ventola, P., Duncan, J., 2021. Braingnn: Interpretable brain graph neural network for fmri analysis. *Medical Image Analysis* 74, 102233.
- Lindquist, M.A., 2008. The statistical analysis of fmri data. *Statistical Science* 23, 439–464.
- Luo, X., Wu, J., Yang, J., Xue, S., Beheshti, A., Sheng, Q.Z., McAlpine, D., Sowman, P., Giral, A., Yu, P.S., 2024. Graph neural networks for brain

- graph learning: A survey, in: Larson, K. (Ed.), Proceedings of the Thirty-Third International Joint Conference on Artificial Intelligence, IJCAI-24, International Joint Conferences on Artificial Intelligence Organization. pp. 8170–8178. Survey Track.
- Luo, Y., Chen, Q., Li, F., Yi, L., Xu, P., Zhang, Y., 2025. Hierarchical feature extraction on functional brain networks for autism spectrum disorder identification with resting-state fmri data. *Neural Networks* 188, 107450.
- Neuhäuser, L., Mellor, A., Lambiotte, R., 2020. Multibody interactions and nonlinear consensus dynamics on networked systems. *Physical Review E* 101.
- Paszke, A., Gross, S., Chintala, S., Chanan, G., Yang, E., DeVito, Z., Lin, Z., Desmaison, A., Antiga, L., Lerer, A., 2017. Automatic differentiation in pytorch, in: NIPS-W.
- Pedregosa, F., Varoquaux, G., Gramfort, A., Michel, V., Thirion, B., Grisel, O., Blondel, M., Prettenhofer, P., Weiss, R., Dubourg, V., Vanderplas, J., Passos, A., Cournapeau, D., Brucher, M., Perrot, M., Duchesnay, E., 2011. Scikit-learn: Machine learning in Python. *Journal of Machine Learning Research* 12, 2825–2830.
- Petri, G., Expert, P., Turkheimer, F., Carhart-Harris, R., Nutt, D., Hellyer, P., Vaccarino, F., 2014. Homological scaffolds of brain functional networks. *Journal of The Royal Society Interface* 11, 20140873.
- Santoro, A., Battiston, F., Lucas, M., Petri, G., Amico, E., 2024. Higher-order connectomics of human brain function reveals local topological signatures of task decoding, individual identification, and behavior. *Nature Communications* 15.
- Santoro, A., Battiston, F., Petri, G., Amico, E., 2023. Higher-order organization of multivariate time series. *Nature Physics* 19, 1–9.
- Shine, J.M., Koyejo, O., Bell, P.T., Gorgolewski, K.J., Gilat, M., Poldrack, R.A., 2015. Estimation of dynamic functional connectivity using multiplication of temporal derivatives. *NeuroImage* 122, 399–407.

- Sizemore, A., Giusti, C., Kahn, A., Vettel, J., Betzel, R., Bassett, D., 2018. Cliques and cavities in the human connectome. *Journal of Computational Neuroscience* 44, 1–31.
- Sporns, O., 2010. *Networks of the Brain*. The MIT Press.
- Su, S., Duta, I., Magister, L.C., Liò, P., 2024. Explaining hypergraph neural networks: From local explanations to global concepts. URL: <https://arxiv.org/abs/2410.07764>, arXiv:2410.07764.
- Talesh Jafadideh, A., Mohammadzadeh Asl, B., 2022. Topological analysis of brain dynamics in autism based on graph and persistent homology. *Computers in Biology and Medicine* 150, 106202.
- Tan, J.B., Müller, E.J., Orlando, I.F., Taylor, N.L., Margulies, D.S., Szeto, J., Lewis, S.J.G., Shine, J.M., O’Callaghan, C., 2023. Abnormal higher-order network interactions in parkinson’s disease visual hallucinations. *Brain* 147, 458–471.
- Tzourio-Mazoyer, N., Landeau, B., DF, P., Crivello, F., Etard, O., Delcroix, N., Mazoyer, B., Marc, J., 2002. Automated anatomical labeling of activations in spm using a macroscopic anatomical parcellation of the mni mri single-subject brain. *NeuroImage* 15, 273–89.
- Veličković, P., Cucurull, G., Casanova, A., Romero, A., Liò, P., Bengio, Y., 2018. Graph attention networks, in: *International Conference on Learning Representations*.
- Wang, M., Huang, J., Liu, M., Zhang, D., 2021. Modeling dynamic characteristics of brain functional connectivity networks using resting-state functional mri. *Medical Image Analysis* 71, 102063.
- Wang, R., Lin, P., Liu, M., Wu, Y., Zhou, T., Zhou, C., 2019. Hierarchical connectome modes and critical state jointly maximize human brain functional diversity. *Phys. Rev. Lett.* 123, 038301.
- Wang, W., Xiao, L., Qu, G., Calhoun, V., Wang, Y.P., Sun, X., 2024a. Multiview hyperedge-aware hypergraph embedding learning for multisite, multiatlas fmri based functional connectivity network analysis. *Medical Image Analysis* 94, 103144.

- Wang, X., Shen, Y., Wei, W., Bai, Y., Li, P., Ding, K., Zhou, Y., Xie, J., Zhang, X., Guo, Z., Wang, M., 2024b. Alterations of regional homogeneity and functional connectivity in different hoehn and yahr stages of parkinson’s disease. *Brain Research Bulletin* 218, 111110.
- Wang, X., Xin, J., Wang, Z., Li, C., Wang, Z., 2022. An evolving hypergraph convolutional network for the diagnosis of alzheimer’s disease. *Diagnostics* 12, 2632.
- Xia, J., Chan, Y., Girish, D., Rajapakse, J., 2025. Interpretable modality-specific and interactive graph convolutional network on brain functional and structural connectomes. *Medical Image Analysis* 102, 103509.
- Xia, M., Wang, J., He, Y., 2013. Brainnet viewer: A network visualization tool for human brain connectomics. *PLoS ONE* 8, e68910. doi:10.1371/journal.pone.0068910.
- Xiao, L., Wang, J., Hosseinzadeh Kassani, P., Zhang, Y., Bai, Y., Stephen, J., Wilson, T., Calhoun, V., Wang, Y.P., 2019. Multi-hypergraph learning based brain functional connectivity analysis in fmri data. *IEEE Transactions on Medical Imaging* PP, 1–1.
- Xu, J., Wang, C., Xu, Z., Li, T., Chen, F., Chen, K., Gao, J., Hu, Q., 2019. Specific functional connectivity patterns of middle temporal gyrus subregions in children and adults with autism spectrum disorder. *Autism Research* 13, 410–422.
- Xu, J., Yang, Y., Huang, D., Gururajapathy, S.S., Ke, Y., Qiao, M., Wang, A., Kumar, H., McGeown, J., Kwon, E., 2023. Data-driven network neuroscience: On data collection and benchmark, in: Oh, A., Naumann, T., Globerson, A., Saenko, K., Hardt, M., Levine, S. (Eds.), *Advances in Neural Information Processing Systems*, Curran Associates, Inc.. pp. 21841–21856.
- Yan, Y., Zhu, J., Duda, M., Solarz, E., Sripada, C.S., Koutra, D., 2019. Groupinn: Grouping-based interpretable neural network for classification of limited, noisy brain data. *Proceedings of the 25th ACM SIGKDD International Conference on Knowledge Discovery & Data Mining* .

- Ye, C., Mori, S., Chan, P., Ma, T., 2019. Connectome-wide network analysis of white matter connectivity in alzheimer’s disease. *NeuroImage: Clinical* 22, 101690.
- Ying, C., Cai, T., Luo, S., Zheng, S., Ke, G., He, D., Shen, Y., Liu, T.Y., 2021. Do transformers really perform badly for graph representation?, in: Ranzato, M., Beygelzimer, A., Dauphin, Y., Liang, P., Vaughan, J.W. (Eds.), *Advances in Neural Information Processing Systems*, Curran Associates, Inc.. pp. 28877–28888.
- Yoshimura, N., Kawamura, M., Masaoka, Y., Homma, I., 2005. The amygdala of patients with parkinson’s disease is silent in response to fearful facial expressions. *Neuroscience* 131, 523–34.
- Yu, S., Jin, S., Li, M., Sarwar, T., Xia, F., 2024. Long-range brain graph transformer, in: Globerson, A., Mackey, L., Belgrave, D., Fan, A., Paquet, U., Tomczak, J., Zhang, C. (Eds.), *Advances in Neural Information Processing Systems*, Curran Associates, Inc.. pp. 24472–24495.
- Zhang, Z., Aggarwal, V., Angelov, P., Jiang, R., 2025. Modeling brain aging with explainable triameter vit: Towards deeper insights into autism disorder. *IEEE journal of biomedical and health informatics* PP.
- Zheng, K., Yu, S., Chen, L., Dang, L., Chen, B., 2024. Bpi-gnn: Interpretable brain network-based psychiatric diagnosis and subtyping. *NeuroImage* 292, 120594.
- Zhi, Y., Huang, T., Liu, S., Li, M., Hu, H., Liang, X., Jiang, Z., Zhu, J., Liu, R., 2024. Correlation between iron deposition and cognitive function in mild to moderate alzheimer’s disease based on quantitative susceptibility mapping. *Frontiers in Aging Neuroscience* 16.
- Zhu, X.W., Zhang, L.L., Zhu, Z.M., Wang, L.Y., Ding, Z., Fang, X.M., 2022. Altered intrinsic brain activity and connectivity in unaffected parents of individuals with autism spectrum disorder: a resting-state fmri study. *Frontiers in Human Neuroscience* 16, 997150.
- Zidan, M., Boban, J., Bjelan, M., Todorović, A., Vujanac Stankov, T., Semnic, M., Boban, N., Kozic, D., 2019. Thalamic volume loss as an early sign of amnesic mild cognitive impairment. *Journal of Clinical Neuroscience* 68.

- Zirh, T., Lenz, F., Reich, S., Dougherty, P., 1998. Patterns of bursting occurring in thalamic cells during parkinsonian tremor. *Neuroscience* 83, 107–21.
- Zou, T., Chen, C., Chen, H., Wang, X., Gan, L., Wang, C., Gao, Q., Zhang, C., Liao, W., Cheng, J., Li, R., 2024. Structural-functional connectivity decoupling in multiscale brain networks in parkinson’s disease. *BMC Neuroscience* 25.

## Appendix A. Ablation study of higher-order features on PPMI and Taowu datasets

To evaluate the effectiveness of more complex signed quadruplet structures and voids (2D holes) formed by triangular faces, we report here a performance comparison with varying feature combinations on the TaoWu and PPMI datasets to have more insight into how HOI-Brain performs on different tasks.

Table A.8: Performance comparison with varying combinations of features on the TaoWu datasets (%). The best results are marked in bold.

Method	Taowu			
	Accuracy	Precision	Recall	F1-score
edge	65.0±5.0	84.8±18.9	55.0±36.7	54.6±17.9
edge+violating triangles+1D loops	70.0±16.9	63.3±37.1	60.0±33.9	60.2±32.9
edge+violating triangles+good quadruplets	67.5±16.9	57.4±33.7	75.0±38.7	62.8±32.4
edge+1D loops+2D voids	67.5±17.0	79.8±17.5	60.0±25.5	62.3±12.8
edge+good quadruplets+2D voids	<b>77.5±9.3</b>	<b>89.3±13.7</b>	70.0±29.1	<u>72.2±17.8</u>
edge+signed good quadruplets+signed 2D voids	<u>77.5±12.3</u>	82.4±9.3	<b>77.5±12.3</b>	<b>75.9±13.9</b>

Table A.9: Performance comparison with varying combinations of features on the PPMI datasets (%). The best results are marked in bold.

Method	PPMI			
	Accuracy	Precision	Recall	F1-score
edge	61.4±7.4	71.6±18.7	45.1±10.1	53.5±8.9
edge+violating triangles+1D loops	57.6±2.4	64.0±9.2	43.8±13.9	49.4±8.1
edge+violating triangles+good quadruplets	60.5±9.2	66.5±19.7	56.4±12.0	58.7±8.3
edge+1D loops+2D voids	63.3±4.2	69.8±11.2	56.9±18.4	59.6±6.1
edge+good quadruplets+2D voids	<u>65.2±4.3</u>	<b>73.1±12.2</b>	<u>58.7±11.1</u>	<u>63.7±4.5</u>
edge+signed good quadruplets+signed 2D voids	<b>66.1±4.0</b>	69.0±4.0	<b>66.3±4.2</b>	<b>64.7±4.7</b>

## Appendix B. Results of hyperparameter analysis on other metrics

In the hyperparameter analysis section, we only reported the influence of the key hyperparameter, the number of clusters, based on the accuracy metric. To better evaluate the impact of this hyperparameter, we additionally present the results of hyperparameter analysis for the other three metrics: precision, recall, and F1 score.

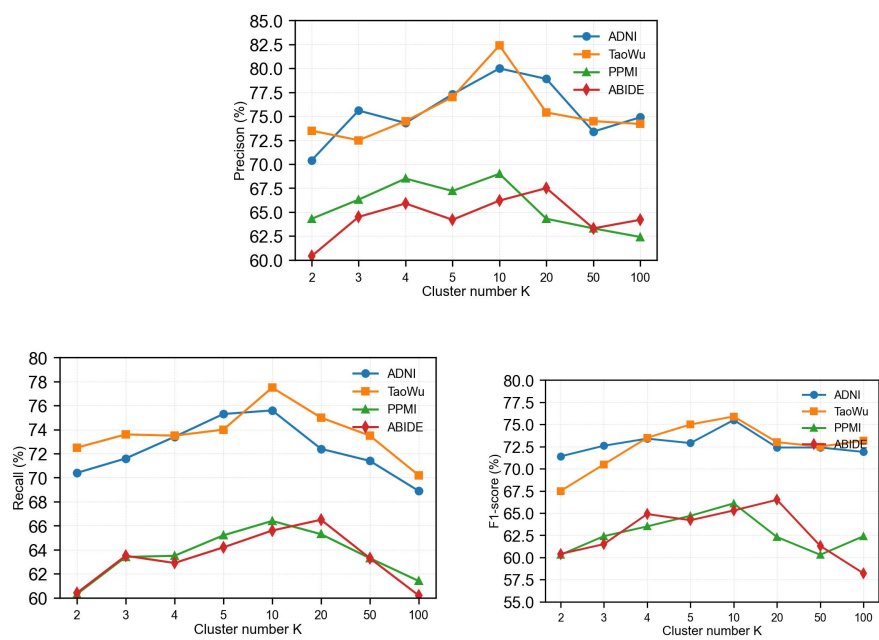


Figure B.18: Influence of the key hyper-parameter, the number of clusters, for model performance on other three metrics.